Available on CMS information server

CMS AN -2019/248

The Compact Muon Solenoid Experiment

Analysis Note

06 November 2019 (v2, 11 December 2020)

Higgs boson mass and on-shell width measurements in the four-lepton final state using full Run 2 data

HZZ mass and on-shell width measurements team

Abstract

The Higgs boson mass and on-shell width are measured in the $\mathrm{H} \to \mathrm{ZZ}^{*} \to 4\ell$ $(\ell = e, \mu)$ decay channel using data collected by the CMS detector at the LHC at a center-of-mass energy $\sqrt{s}$ = 13during Run 2, corresponding to an integrated luminosity of 137 .fb^{-1}

Contents

1 Introduction

On the 4th of July 2012, ATLAS and CMS collaborations announced the discovery of a new particle compatible with the Standard Model Higgs boson [1]. Since then, many efforts have been profused to better studies its properties.

Currently, the most precise Higgs boson mass measurement has been done with CMS detector, combining $\mathrm{H} \rightarrow \gamma\gamma$ and $\mathrm{H} \rightarrow \mathrm{ZZ}^* \rightarrow 4\ell$ channels, Run 1 at 7 and 8 TeV, and 13 TeV 2016 data, corresponding to respectively 5, 20 and 36 fb^{-1}: $125.38 \pm 0.14(\pm 0.11)$ GeV [2]. Latest ATLAS collaboration results have been obtained using Full Run 2 data, corresponding to an integrated luminosity of 139 fb^{-1}, studying $\mathrm{H} \rightarrow \mathrm{ZZ}^* \rightarrow 4\ell$ channel: $124.92^{+0.21}_{-0.20}$ $[0.19(stat)^{+0.09}_{-0.06}(syst)]$ GeV [3].

Concerning the Higgs boson width, comparing on-shell and off-shell production, CMS was able to set for the first time a lower bound: $3.2^{+2.8}_{-2.2}$ MeV [4]. Looking only at the on-shell production, the width is constrained to be $\Gamma_H <$1.10 GeV, at 95% CL [5], limited by mass resolution.

This analysis note deals with the measurement of the Higgs boson mass and width (looking only at the on-shell production), in the $\mathrm{H} \rightarrow \mathrm{ZZ}^* \rightarrow 4\ell$ decay channel, using 137 fb^{-1} pp collision data collected at $\sqrt{s}$=13 TeV, with the CMS experiment at the LHC during 2016-2018.

2 Datasets

This analysis uses the same data sets for data as in HIG-19-001. The full lists can be consulted in [6]. Simulated data sets for signal and background (same as [6]) are listed in Table 1, 2, 3.

Signal dataset name	XS × BR [pb]
GluGluHToZZTo4L_M125_13TeV_powheg2_JHUGenV709_pythia8[1]	0.01333521
VBF_HToZZTo4L_M125_13TeV_powheg2_JHUGenV709_pythia8[1]	0.001038159
WplusH_HToZZTo4L_M125_13TeV_powheg2-minlo-HWJ_JHUGenV709_pythia8[1]	0.000146235
WminusH_HToZZTo4L_M125_13TeV_powheg2-minlo-HWJ_JHUGenV709_pythia8[1]	0.0002305562
ZH_HToZZ_4LFilter_M125_13TeV_powheg2-minlo-HZJ_JHUGenV709_pythia8[1]	0.000662058
ttH_HToZZ_4LFilter_M125_13TeV_powheg2_JHUGenV709_pythia8[1]	0.0003901903

Background dataset name	XS × BR [pb]
ZZTo4L_13TeV_powheg_pythia8[1]	1.256
GluGluToContinToZZTo4e_13TeV_MCFM701_pythia8[1]	0.00158549
GluGluToContinToZZTo4mu_13TeV_MCFM701_pythia8[1]	0.00158549
GluGluToContinToZZTo4tau_13TeV_MCFM701_pythia8[1]	0.00158549
GluGluToContinToZZTo2e2mu_13TeV_MCFM701_pythia8[1]	0.00319142
GluGluToContinToZZTo2e2tau_13TeV_MCFM701_pythia8[1]	0.00319142
GluGluToContinToZZTo2mu2tau_13TeV_MCFM701_pythia8[1]	0.00319142

Table 1: 2016 samples.
[1]: "RunIISummer16MiniAODv2-PUMoriond17_80X_mcRun2_asymptotic_2016_TrancheIV_v6"

Signal dataset name	XS × BR [pb]
GluGluHToZZTo4L_M125_13TeV_powheg2_JHUGenV7011_pythia8[2]	0.01333521
VBF_HToZZTo4L_M125_13TeV_powheg2_JHUGenV7011_pythia8[2]	0.001038159
WplusH_HToZZTo4L_M125_13TeV_powheg2-minlo-HWJ_JHUGenV7011_pythia8[2]	0.000146235
WminusH_HToZZTo4L_M125_13TeV_powheg2-minlo-HWJ_JHUGenV7011_pythia8[2]	0.0002305562
ZH_HToZZ_4LFilter_M125_13TeV_powheg2-minlo-HZJ_JHUGenV7011_pythia8[2]	0.000662058
ttH_HToZZ_4LFilter_M125_13TeV_powheg2_JHUGenV7011_pythia8[2]	0.0003901903

Background dataset name	XS *imes* BR [pb]
ZZTo4L_13TeV_powheg_pythia8[2]	1.256
GluGluToContinToZZTo4e_13TeV_MCFM701_pythia8[2]	0.00158549
GluGluToContinToZZTo4mu_13TeV_MCFM701_pythia8[2]	0.00158549
GluGluToContinToZZTo4tau_13TeV_MCFM701_pythia8[2]	0.00158549
GluGluToContinToZZTo2e2mu_13TeV_MCFM701_pythia8[2]	0.00319142
GluGluToContinToZZTo2e2tau_13TeV_MCFM701_pythia8[2]	0.00319142
GluGluToContinToZZTo2mu2tau_13TeV_MCFM701_pythia8[2]	0.00319142

Table 2: 2017 samples.
[2]: "RunIIFall17MiniAODv2-PU2017_12Apr2018_94X_mc2017_realistic_v14"

3 Objects

This analysis follows the same object definition as in HIG-19-001 for each year. The corresponding information about objection definitions and scale factor can be found in [6].
This section will be filled when UL samples will be ready.

Signal dataset name	XS *imes* BR [pb]
GluGluHToZZTo4L_M125_13TeV_powheg2_JHUGenV7011_pythia8[3]	0.01333521
VBF_HToZZTo4L_M125_13TeV_powheg2_JHUGenV7011_pythia8[3]	0.001038159
WplusH_HToZZTo4L_M125_13TeV_powheg2-minlo-HWJ_JHUGenV7011_pythia8[3]	0.000146235
WminusH_HToZZTo4L_M125_13TeV_powheg2-minlo-HWJ_JHUGenV7011_pythia8[3]	0.0002305562
ZH_HToZZ_4LFilter_M125_13TeV_powheg2-minlo-HZJ_JHUGenV7011_pythia8[3]	0.000662058
ttH_HToZZ_4LFilter_M125_13TeV_powheg2_JHUGenV7011_pythia8[3]	0.0003901903

Background dataset name	XS *imes* BR [pb]
ZZTo4L_TuneCP5_13TeV_powheg_pythia8[3]	1.256
GluGluToContinToZZTo4e_13TeV_MCFM701_pythia8[3]	0.00158549
GluGluToContinToZZTo4mu_13TeV_MCFM701_pythia8[3]	0.00158549
GluGluToContinToZZTo4tau_13TeV_MCFM701_pythia8[3]	0.00158549
GluGluToContinToZZTo2e2mu_13TeV_MCFM701_pythia8[3]	0.00319142
GluGluToContinToZZTo2e2tau_13TeV_MCFM701_pythia8[3]	0.00319142
GluGluToContinToZZTo2mu2tau_13TeV_MCFM701_pythia8[3]	0.00319142

Table 3: 2018 samples.
[3]: "RunIIAutumn18MiniAOD-102X_upgrade2018_realistic_v15"

3.1 Electrons

3.2 Muons

3.3 Photons

3.4 Jets and MET

4 Event Selection

Event selection follows the same step as in [6]: trigger selection, vertex selection, selection of the four leptons and finally selection of the ZZ candidate. In case that more than one ZZ candidate is found to fullfil the selection, the one with the highest value of D^{kin}_{bkg} is chosen.

5 Signal modelling

5.1 Signal normalization

The normalization of the Higgs boson signal is obtained, from simulation, looking at the expected signal yields in the range [105, 140] GeV, for five simulated mass points (120, 124, 125, 126 and 130 GeV). A second order polynomial function is used to extract the dependence of the normalization from m_H. Fits are performed separately for each production mode, for each decay channel and for each year. Examples of the fits can be observed in Figure 1, 2, 3

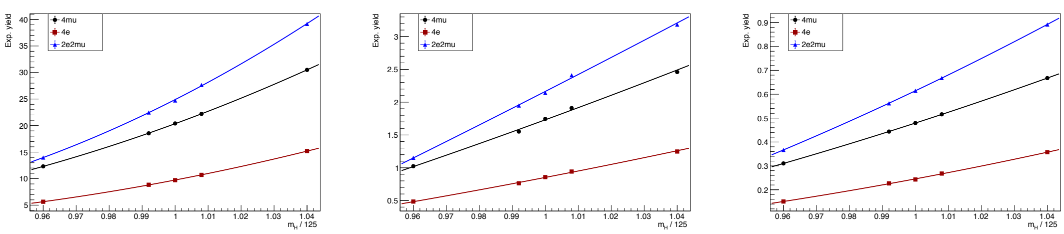

Figure 1: Normalization fit in 2016, for different decay channels, as a function of mass, for ggH on the left, VBF in the middle, WH on the right.

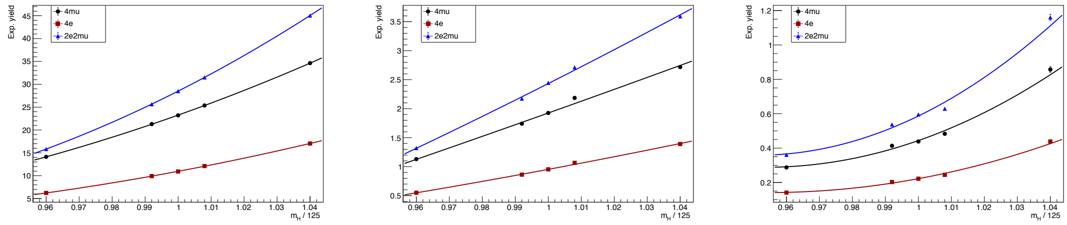

Figure 2: Normalization fit in 2017, for different decay channels, as a function of mass, for ggH on the left, VBF in the middle, ZH on the right.

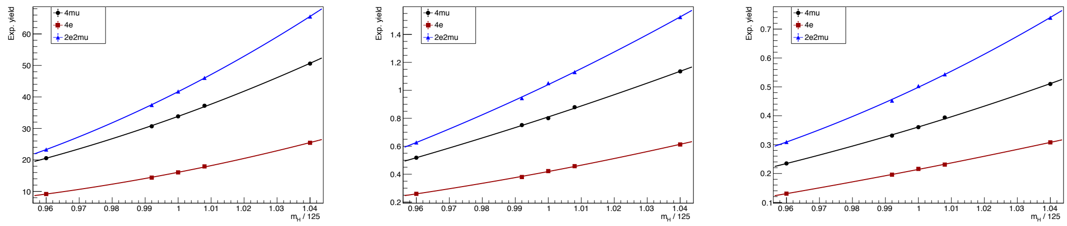

Figure 3: Normalization fit in 2018, for different decay channels, as a function of mass, for ggH on the left, WH in the middle, ttH on the right.

5.2 Signal parametrization

5.2.1 For mass measurement

The signal lineshape is obtained from the fit of the Higgs boson mass distribution, in the range [105, 140] GeV, using a double-sided Crystal Ball (DSCB) function. Fit parameters are derived as a function of mass, using a second order polynomial:

$$param_{DSCB} = a + b\,(m_H - 125) + c\,(m_H - 125)^2$$

The initial value for the parameters (a value) is obtained from the fit of the 125 GeV sample; the first and second order term instead (b and c values) are obtained from a simultaneous fit of various mass points (120, 124, 126, 130 GeV), including 125 GeV sample.
The fit is performed separately, for each production mode, for each decay channel, in each year.
To take into account the "non resonant" contribution in the case of VH production mode, the DSCB is convoluted with a Landau function that describes the possibility for a lepton from the Higgs boson decay to be lost or not selected.
Examples of the fit procedures are shown in Figure 4, 5, 6 for 125 GeV sample, and in Figure 7, 8, 9, 10, 11 and 12, for the simultaneous fits.

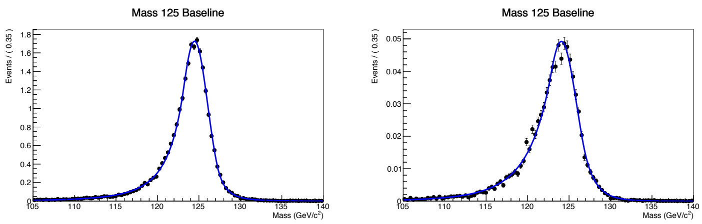

Figure 4: 125 GeV fit in 2016: 2e2μ ggF on the left, 4e VBF on the right.

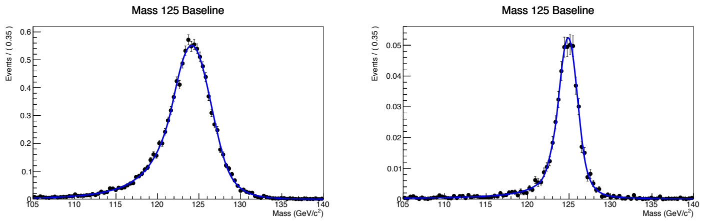

Figure 5: 125 GeV fit in 2017: 4e ggF on the left, 4μ WH on the right.

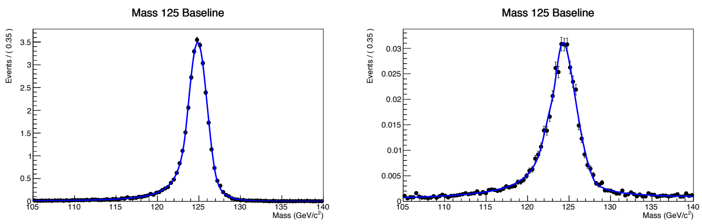

Figure 6: 125 GeV fit in 2018: 4μ ggF on the left, 2e2μ ttH on the right.

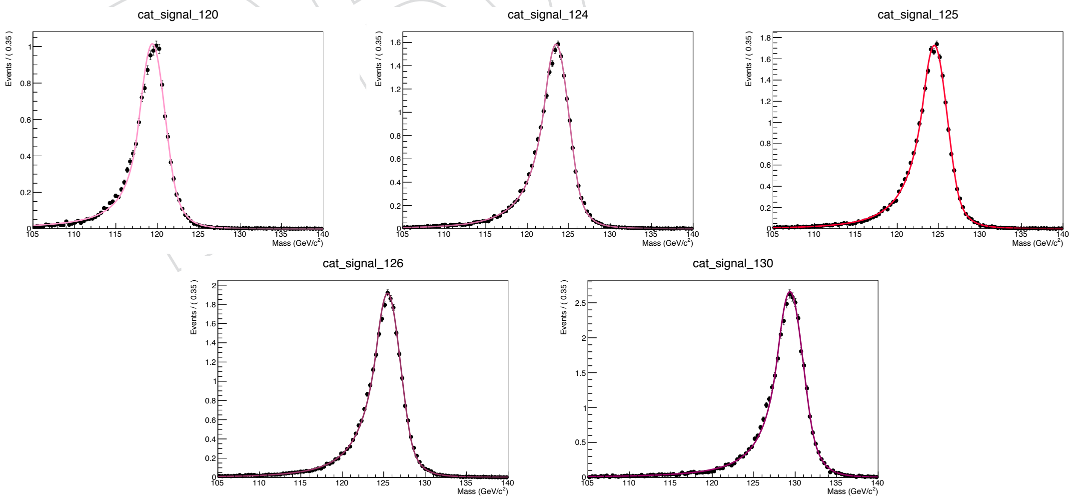

Figure 7: Simultaneous fit for ggH production mode, in 2016, for different mass points, in 2e2μ final state.

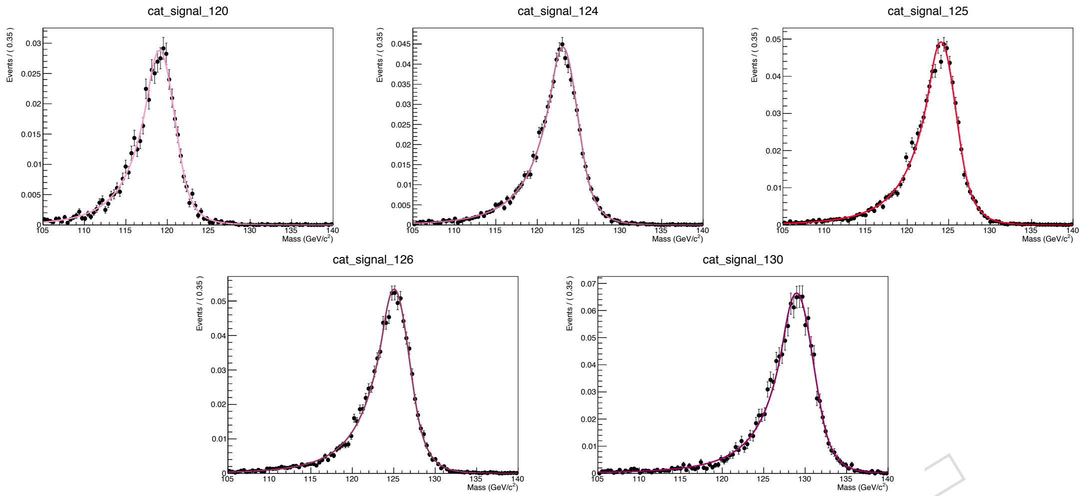

Figure 8: Simultaneous fit for VBF production mode, in 2016, for different mass points, in 4e final state.

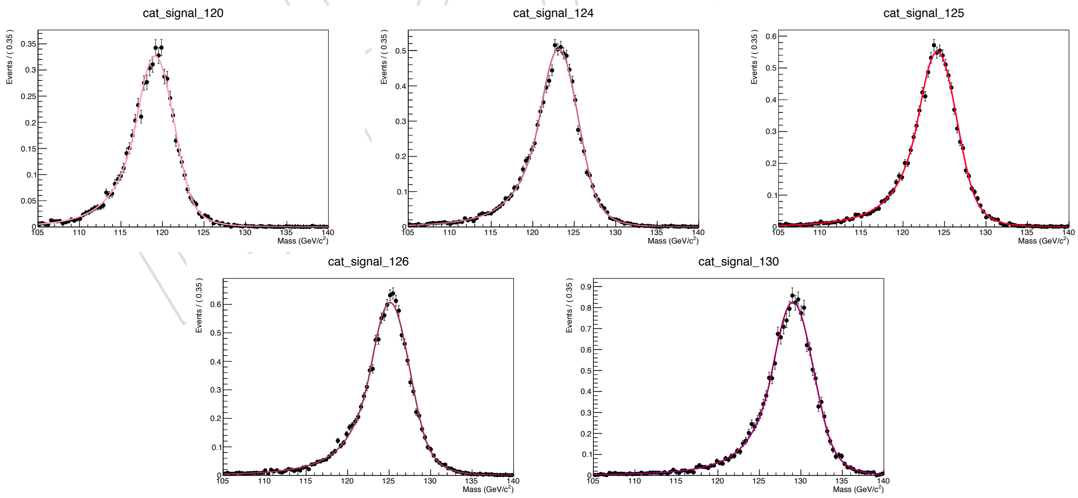

Figure 9: Simultaneous fit for ggH production mode, in 2017, for different mass points, in 4e final state.

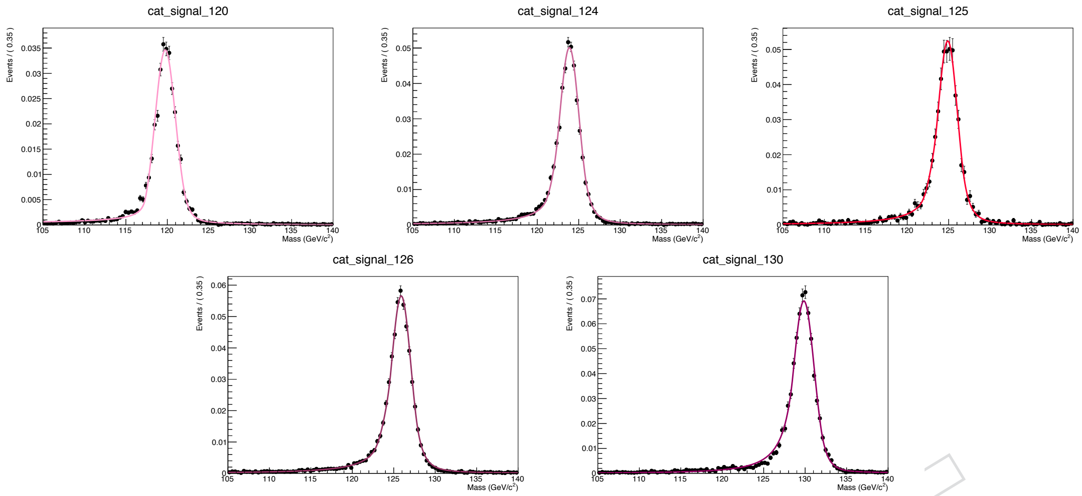

Figure 10: Simultaneous fit for WH production mode, in 2017, for different mass points, in 4μ final state.

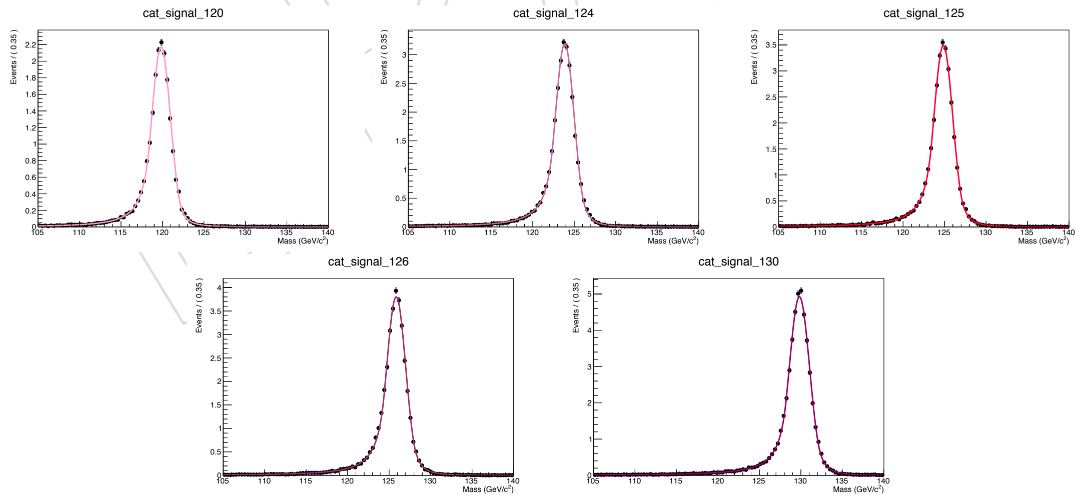

Figure 11: Simultaneous fit for ggH production mode, in 2018, for different mass points, in 4μ final state.

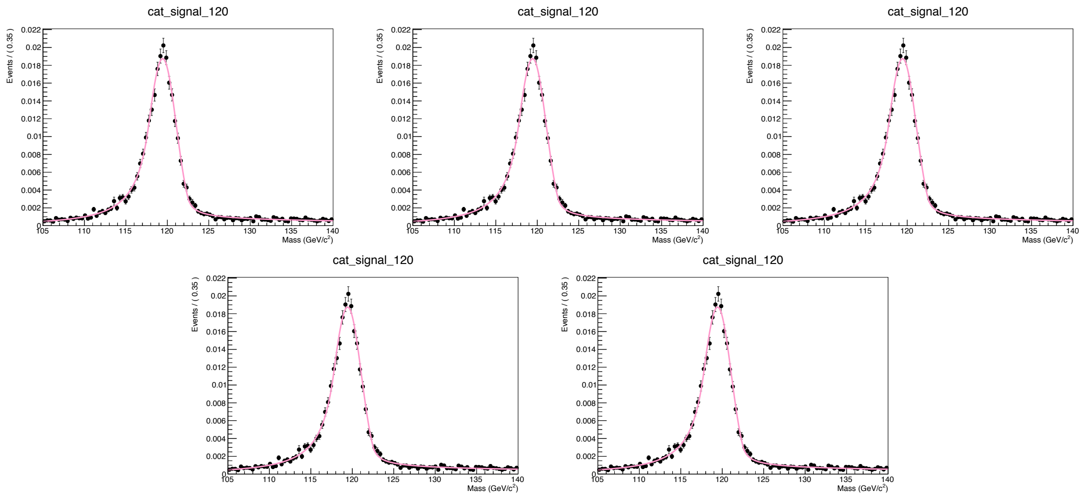

Figure 12: Simultaneous fit for ggH production mode, in 2018, for different mass points, in $2e2\mu$ final state.

5.2.2 For on-shell width measurement

For on-shell width measurement, the signal lineshape has been obtained from the fit of the 125 GeV ggF sample in the three different final states. Examples of the fit procedures are shown in Figure 13, 14, 15.

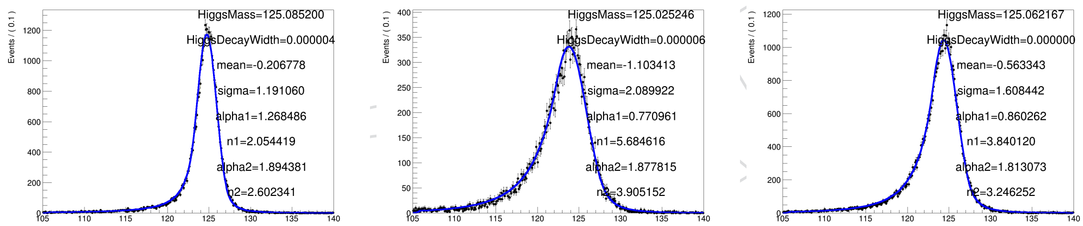

Figure 13: Signal lineshape for 2016: 4μ on left, 4e in the middle, $2e2\mu$ on right.

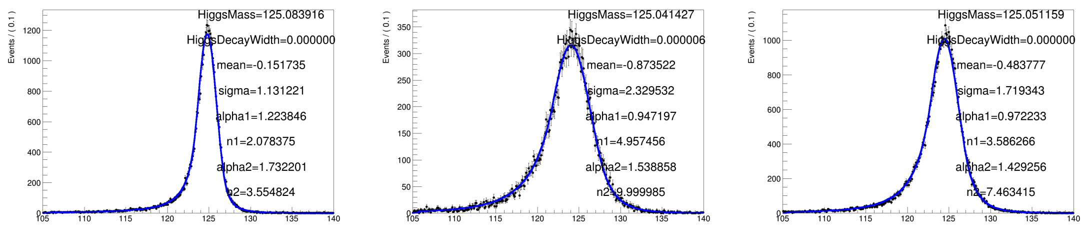

Figure 14: Signal lineshape for 2017: 4μ on left, 4e in the middle, $2e2\mu$ on right.

6 Expected m_{H} uncertainties using a 1D pdf

This section will present the expected result on the Higgs boson mass measurement in case of perfect background rejection (no-bkg) and neglecting systematic uncertainties (no-syst).

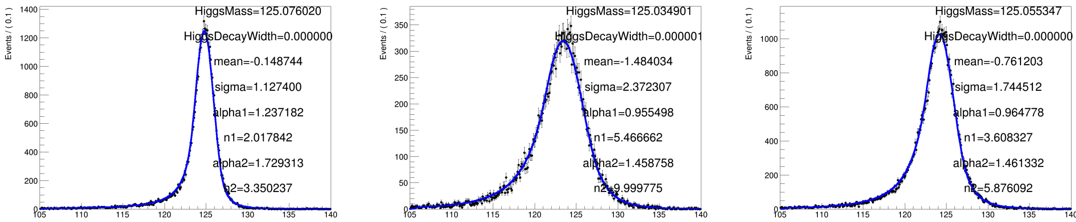

Figure 15: Signal lineshape for 2018: 4μ on left, 4e in the middle, $2e2\mu$ on right.

6.1 Building the 1D pdf

Higgs boson mass measurement is firstly extracted from a one-dimnetional likelihood function $\mathcal{L}(m_{4\ell}|m_H)$, where m_H is fixed to the value of 125 GeV. The model and the normalisation used for the signal are described in 5.1.

6.2 Expected m_{H} measurement uncertainties (MC)

The expected m_{H} measurement uncertainty, split for different final state, is reported in Table 4.

Expected uncertainty	4μ	4e	$2e2\mu$	$2\mu2e$	inclusive	Stat only
1D model	-	-	-	-	-	-

Table 4: Higgs boson mass uncertainty measured with 1D model. All mass values are given in GeV. The uncertainties are the total statistical plus systematic uncertainty, unless otherwise stated.

7 Expected m_{H} uncertainties using a 2D pdf

7.1 Event-by-event mass uncertainty: $D_{m_{4\ell}}$

7.1.1 Motivation

Individual lepton uncertainty on momentum measurement can be predicted on a per-lepton basis. In the case of muons, the full error matrix is obtained using muon track fit; for the electrons, instead, the momentum error is estimated from the combination of the ECAL and tracker measurement, neglecting the uncertainty on the track direction from the GSF fit.
The uncertainty on the kinematics at the per-lepton level is then propagated to the four-lepton case to predict the mass error on an event-by-event basis, using the following approach.
Each δm_i, corresponding to individual lepton momentum variation, is calculated separately and then the measured resolution on the invariant mass of the four leptons is taken as the quadrature sum of the four individual δm_i:

$$m_0 = F(p_{T1}, \phi_1, \eta_1; p_{T2}, \phi_2, \eta_2; p_{T3}, \phi_3, \eta_3; p_{T4}, \phi_4, \eta_4)$$

$$\delta m_i = F(...; p_{Ti} + \delta p_{Ti}, \phi_i, \eta_i; ...) - m_0$$

$$\delta m = \sqrt{\delta m_1^2 + \delta m_2^2 + \delta m_3^2 + \delta m_4^2}$$

Figure 16 shows full error matrix $(\eta, \delta p_T / p_T)$ for muons and electrons.

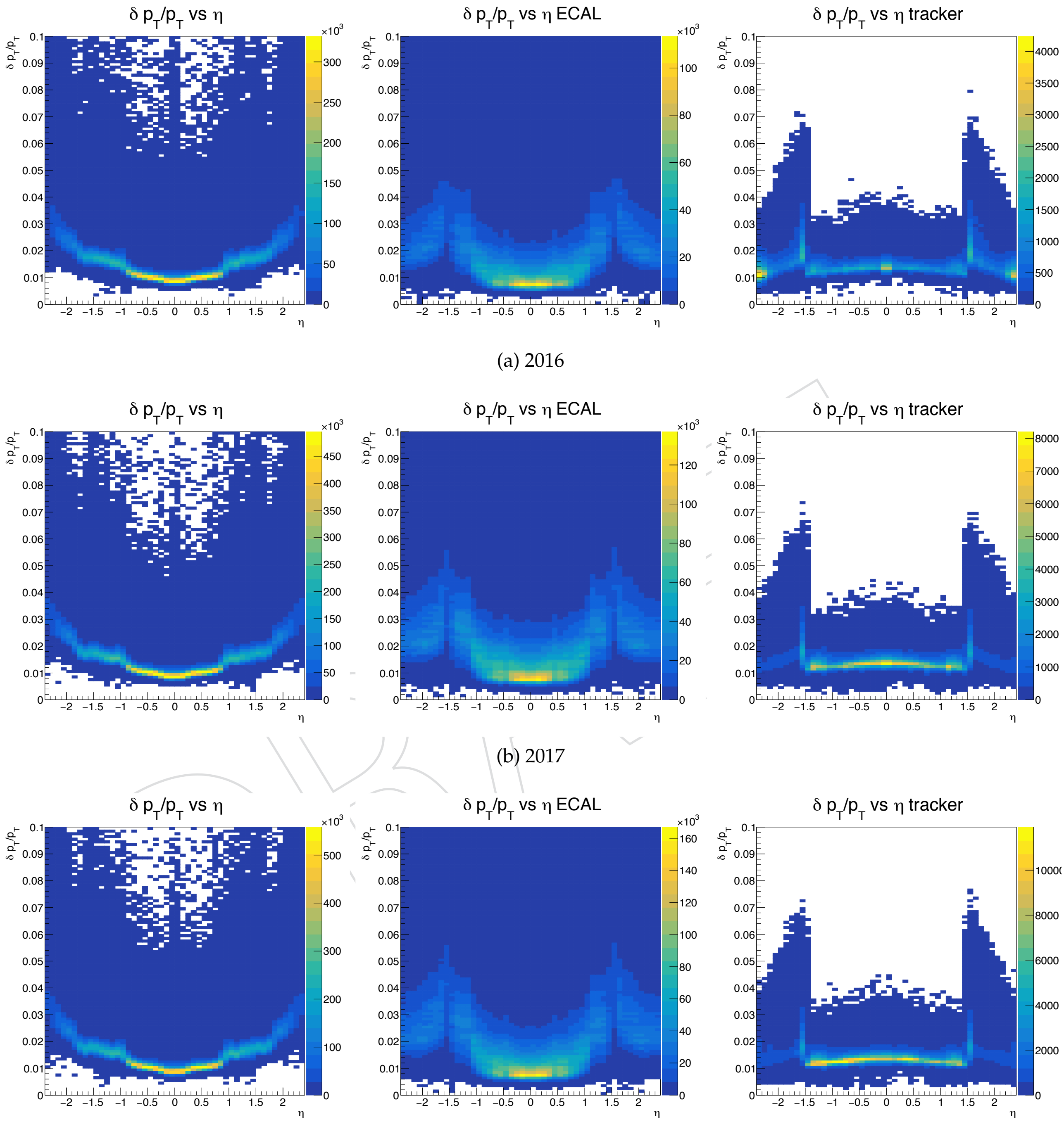

(a) 2016

(b) 2017

(c) 2018

Figure 16: Scatter plot of the relative lepton p_{T} error vs η for muons (left), ECAL driven electrons (middle) and tracker driven electrons (right).

Starting from these distributions, corrections to momentum uncertainty are derived for muons in several mutual $|\eta|$ bins, and for tracker and ECAL driven electron in bins of $\delta p_T/p_T$ vs $|\eta|$. The scatter plots $\delta p_T/p_T$ vs p_T are shown in Figure 17, 18 and 19.

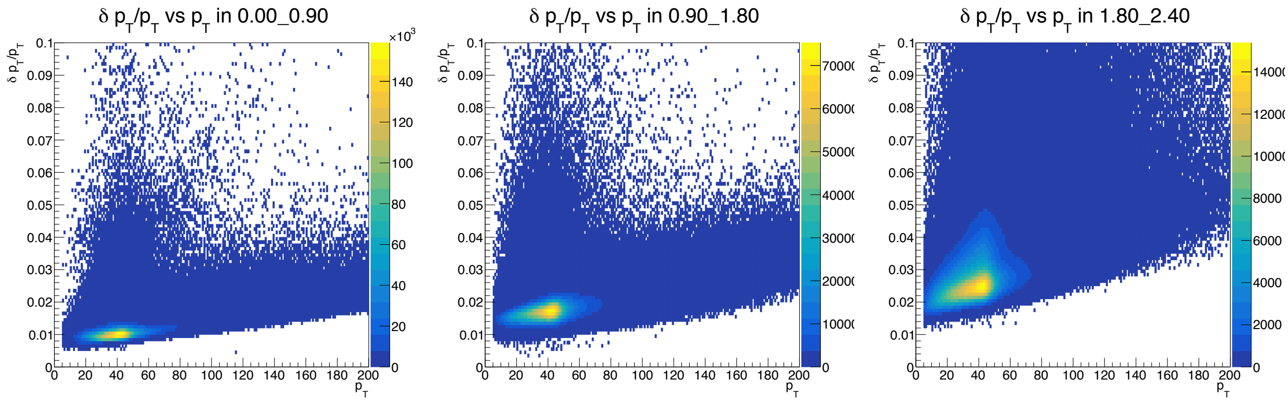

(a) 2016

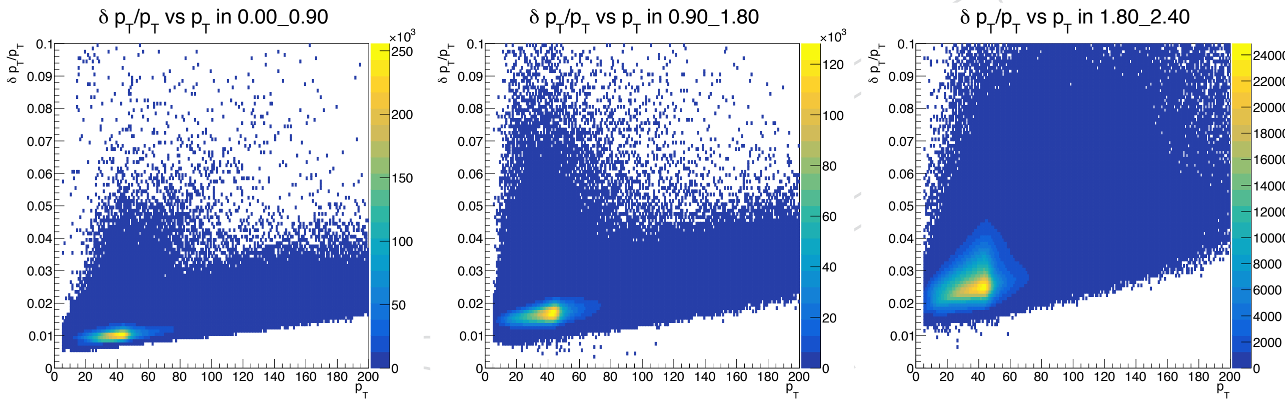

(b) 2017

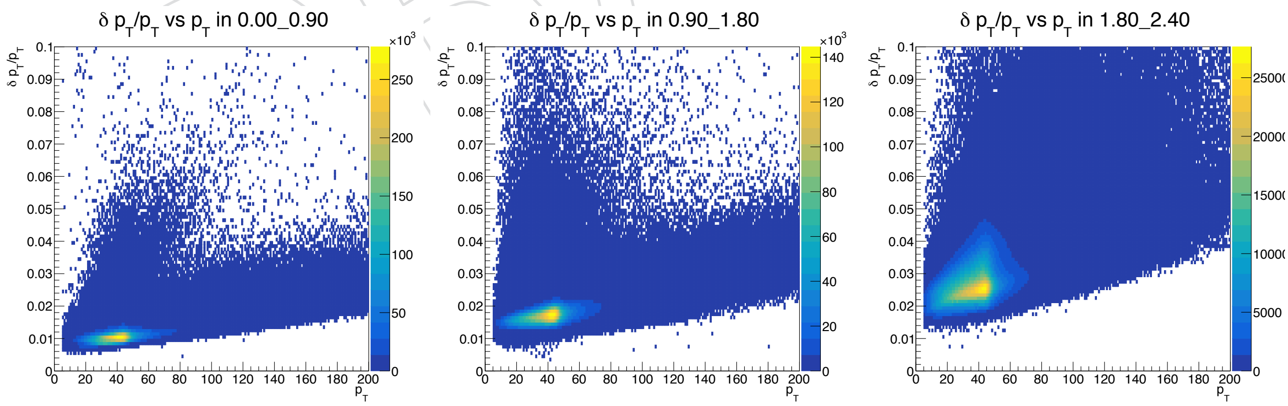

(c) 2018

Figure 17: Scatter plot of the relative lepton p_{T} error vs p_{T} for muons, in different $|\eta|$ regions.

7.1.2 Model and procedure to derive corrections

To derive the corrections (λ), the dilepton mass $m_{\ell\ell}$ is fitted twice with a Breit-Wigner (BW) convoluted with a Crystal Ball (CB), plus exponential function (EXP). In this model, the BW

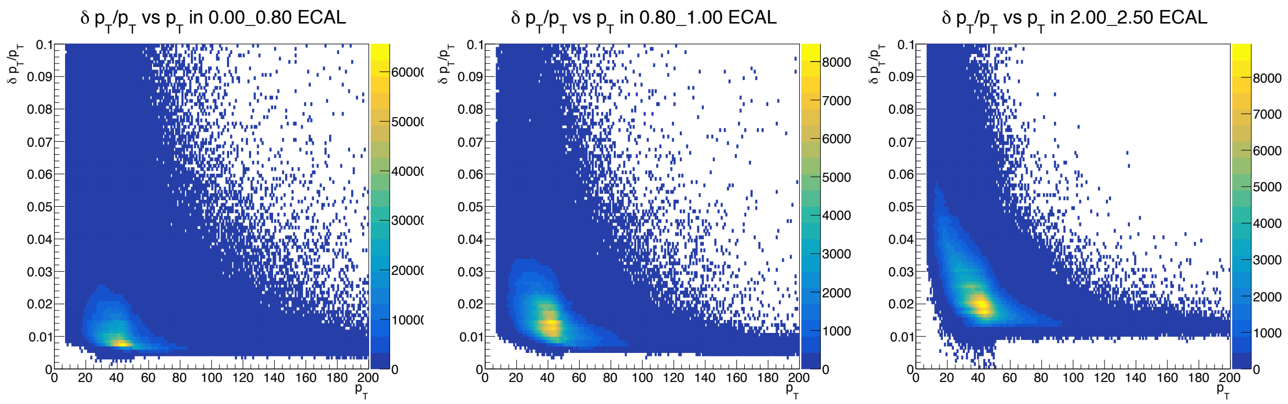

(a) 2016

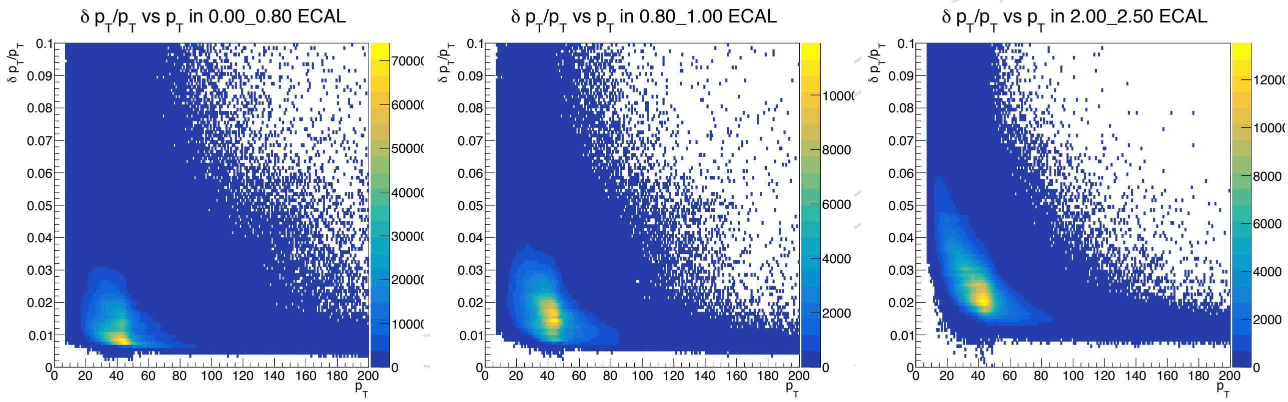

(b) 2017

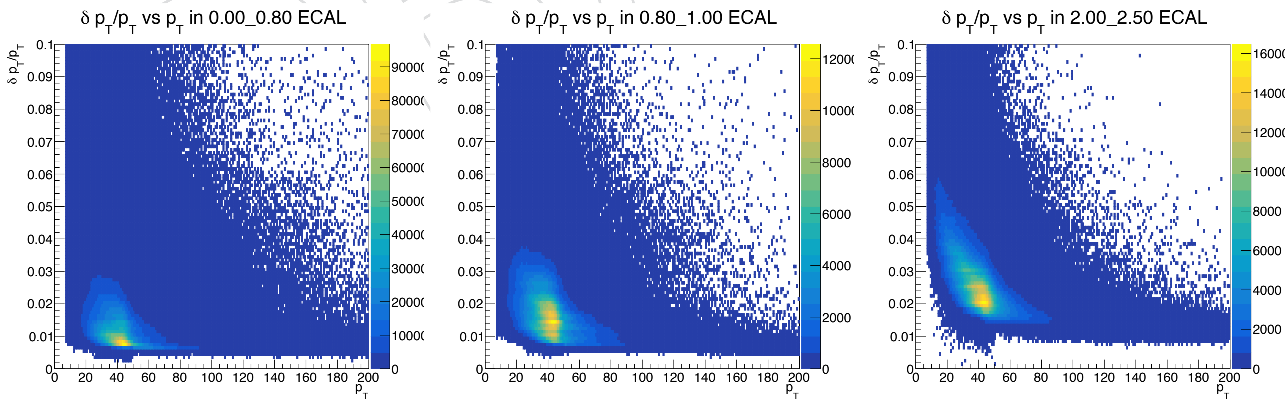

(c) 2018

Figure 18: Scatter plot of the relative lepton p_{T} error vs p_{T} for ECAL electrons, in different $|\eta|$ regions.

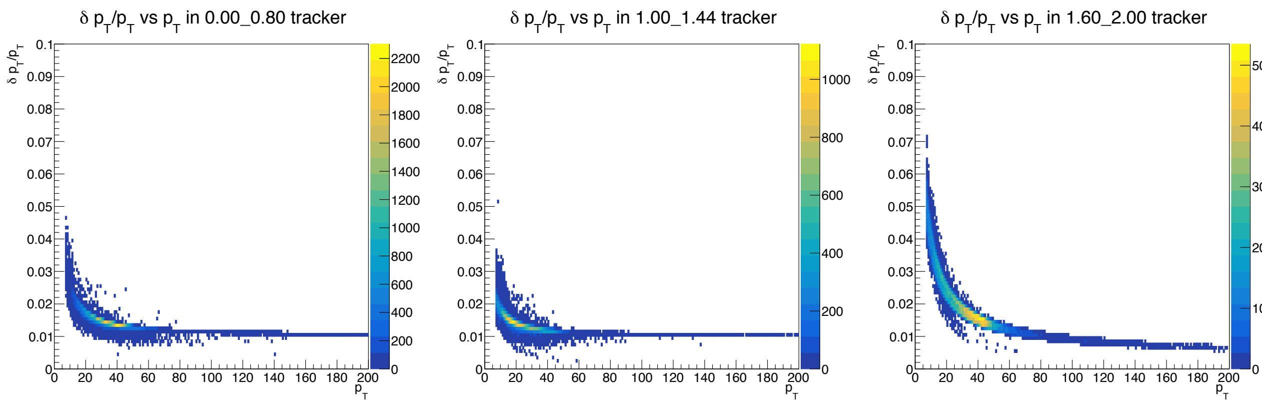

(a) 2016

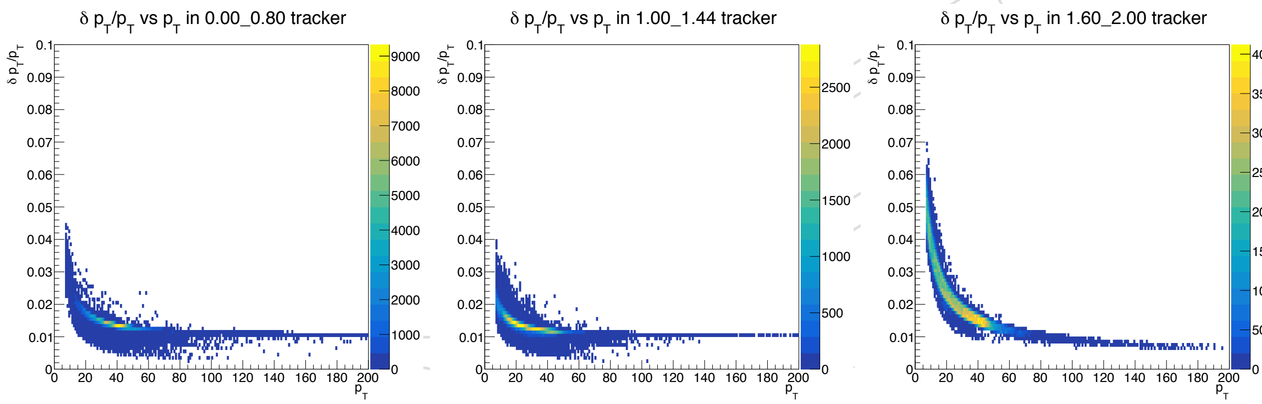

(b) 2017

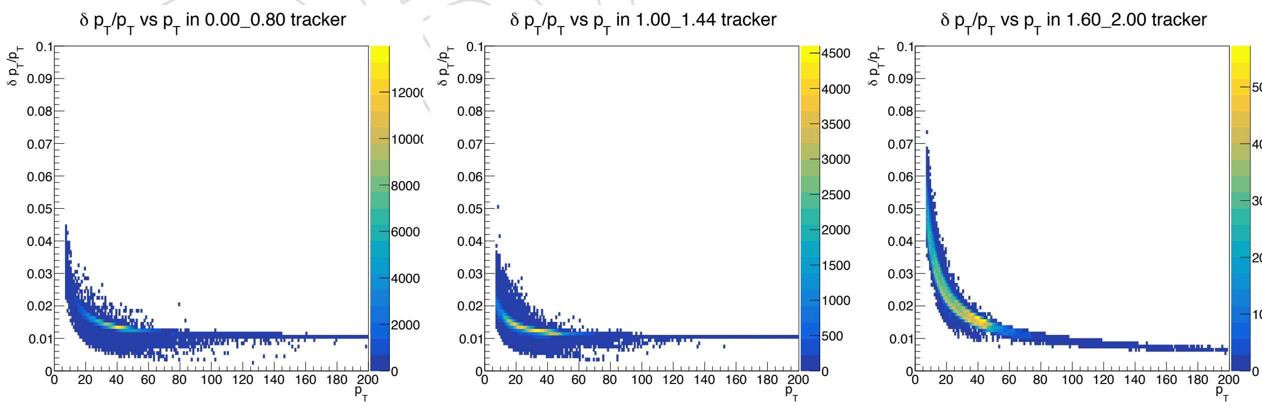

(c) 2018

Figure 19: Scatter plot of the relative lepton p_{T} error vs p_{T} for tracker electrons, in different $|\eta|$ regions.

represents true m_Z shape, the CB simulates the detector effect, and the EXP describes the background. When deriving corrections, mean and sigma of Z's BW shape have been set to PDG values ($mean_Z$ = 91.19 GeV, σ_Z = 2.49 GeV [7]). The fit is done in the mass range [60, 120] GeV, using only e^+e^- or $\mu^+\mu^-$ pairs.
The first fit is used to fix all the parameters of the functions but the σ of the CB which is replaced in the second fit by $\lambda \times \delta_{m_Z}$, where λ is the floated parameter of the fit.

The summary of λ correction factors for electrons and muons is presented in Table 5.

	2016		**2017**		**2018**	
	MC	**Data**	**MC**	**Data**	**MC**	**Data**
			Muons			
$0 < \|\eta\| < 0.9$	1.217	1.236	1.184	1.200	1.177	1.200
$0.9 < \|\eta\| < 1.8$	1.252	1.233	1.254	1.225	1.225	1.217
$1.8 < \|\eta\| < 2.4$	1.214	1.146	1.228	1.161	1.210	1.145
			ECAL electrons			
$0 < \|\eta\| < 0.8$ and $\delta p_T / p_T < 0.01$	2.006	1.893	2.086	2.030	2.054	1.914
$0 < \|\eta\| < 0.8$ and $0.01 < \delta p_T / p_T < 0.015$	1.590	1.575	1.698	1.680	1.701	1.635
$0 < \|\eta\| < 0.8$ and $0.015 < \delta p_T / p_T < 0.025$	1.406	1.373	1.426	1.450	1.447	1.467
$0 < \|\eta\| < 1$ and $0.025 < \delta p_T / p_T < 1$	1.517	1.531	1.481	1.521	1.560	1.569
$1 < \|\eta\| < 2.5$ and $\delta p_T / p_T < 0.02$	2.116	2.002	2.305	2.210	2.324	2.228
$1 < \|\eta\| < 2.5$ and $0.02 < \delta p_T / p_T < 0.03$	1.645	1.623	1.815	1.795	1.787	1.759
$1 < \|\eta\| < 2.5$ and $0.03 < \delta p_T / p_T < 0.04$	1.472	1.489	1.568	1.560	1.468	1.509
$1 < \|\eta\| < 2.5$ and $0.04 < \delta p_T / p_T < 0.06$	1.374	1.448	1.414	1.606	1.378	1.477
$0.8 < \|\eta\| < 1$ and $\delta p_T / p_T < 0.025$	1.149	1.203	1.196	1.241	1.180	1.286
$1 < \|\eta\| < 2.5$ and $0.06 < \delta p_T / p_T < 1$	1.099	1.221	1.171	1.331	1.123	1.272
			tracker electrons			
$0 < \|\eta\| < 1.44$	1.619	1.872	2.382	2.115	2.120	1.936
$1.44 < \|\eta\| < 1.6$	6.452	5.900	6.572	7.056	5.613	5.524
$1.6 < \|\eta\| < 2$	2.732	2.826	3.430	2.846	3.204	3.016
$2 < \|\eta\| < 2.5$	3.010	3.081	3.963	3.817	4.110	3.762

Table 5: p_T error corrections for muons and electrons in different kinematic region. For each year, MC is on the left, data on the right.

7.1.3 Validation of corrections (MC, data)

A closure test is performed to validate correction derived for lepton p_T error.
First, events are divided according to different predicted $\delta m_Z / m_Z$ ranges before corection. Then, in each bin, the dilepton mass distribution is fitted using a BW convoluted with CB plus exponential function, to get δm_Z^{fit} (measured m_Z resolution). Finally the average predicted δm_Z is calculated in each $\delta m_Z / m_Z$ bin before and after the correction factor for lepton p_T error is applied (predicted m_Z resolution).
In the closure plot, it is expected to see δm_Z gets closer to δm_Z^{fit} after correction, and the points should stay in a band which is 20% around diagonal line, which is the uncertainty assigned to the resolution in the previous analysis [5]. This closure test is shown in Figure 20 for muons and in Figure 21 for electrons. A further check has been also performed, looking at the closure test of the predicted four lepton mass resolution compared to the fitted four lepton mass resolution using ggF signal MC samples once the corrections derived using Z events are applied.

After applying correction, measured m_{4l} resolution gets closer to the prediction. This closure test is shown for three different final states in Figure 22.

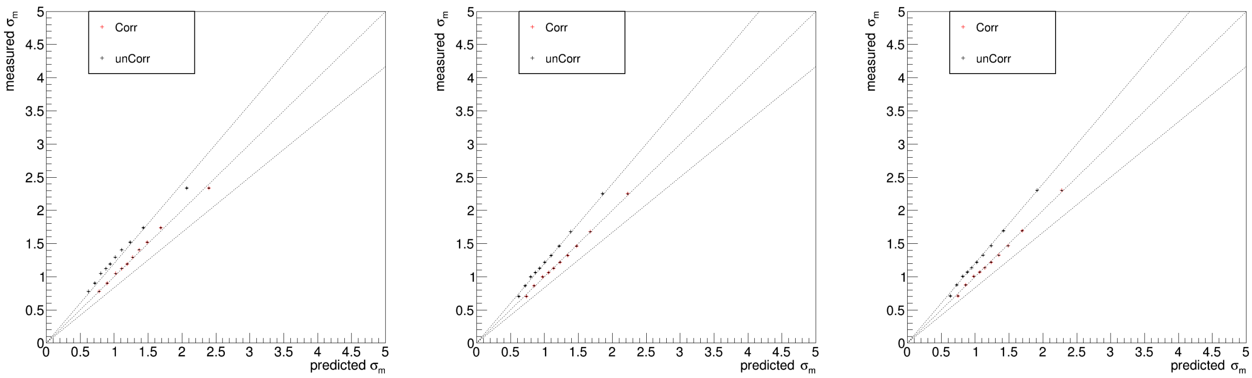

(a) MC

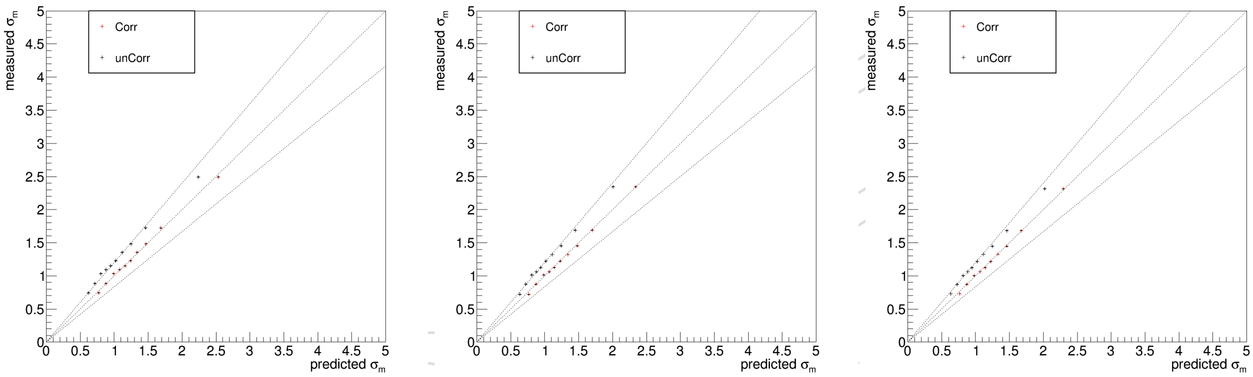

(b) Data

Figure 20: Validation of the per-event mass uncertainties from Z events in MC (top) and Data (bottom) in dimuon channel in 2016 (left), 2017 (middle) and 2018 (right). 20% reference band is also shown.

7.2 Result using 2D model

The mass error uncertainty evaluated in 7.1 is combined with the four-lepton mass to built a two-dimentional likelihood function, $\mathcal{L}(m_{4\ell}, D_{m_{4\ell}}|m_H)$, where again m_H is fixed to the value of 125 GeV.
The expected m_{H} measurement uncertainty, in case of no-bkg and no-syst, split for different final state, is reported in Table 6, compared with 1D result.

8 Expected m_{H} uncertainties using a 2D pdf with p_{T} improvements.

8.1 New muon reconstruction improvements

This section will describe new approaches developed to improvement muon reconstruction. Perfect reconstruction of a muon track would show the track intersecting the vertex from which the muon came. However, track reconstruction is imperfect causing a muon p_{T} mis-measurement. Thus muon tracks will have a non-zero offset relative to the originating vertex.

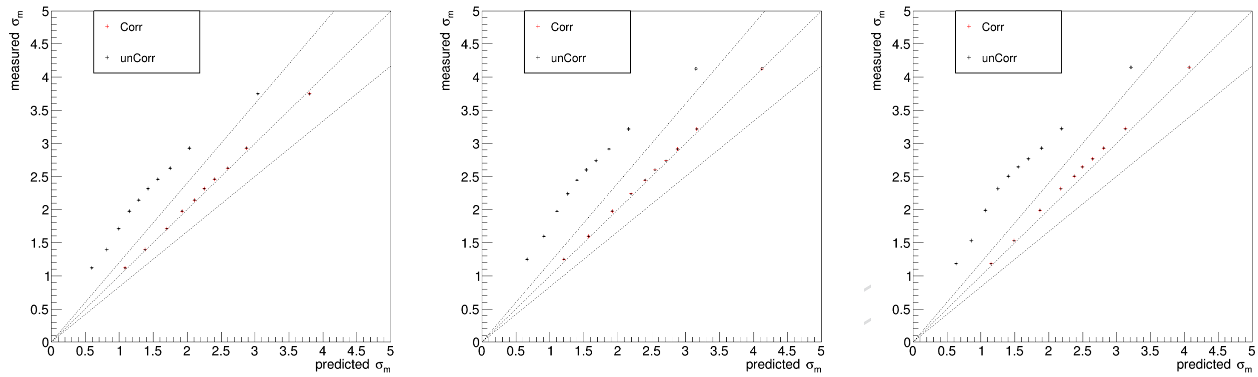

(a) MC

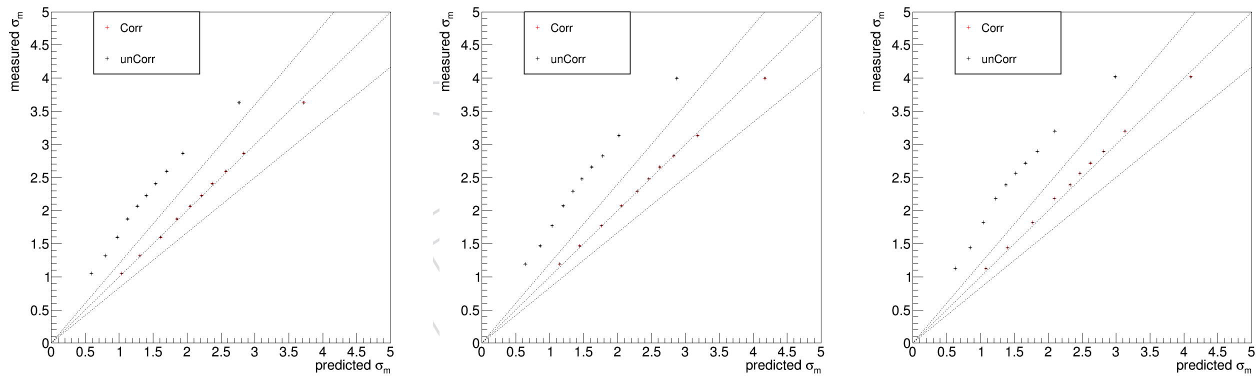

(b) Data

Figure 21: Validation of the per-event mass uncertainties from Z events in MC (top) and Data (bottom) in dielectron channel in 2016 (left), 2017 (middle) and 2018 (right). 20% reference band is also shown.

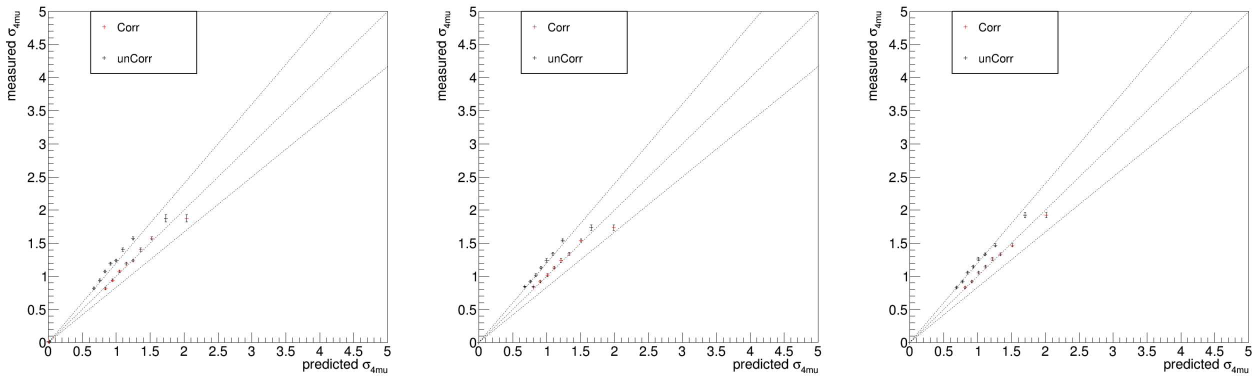

(a) 4μ

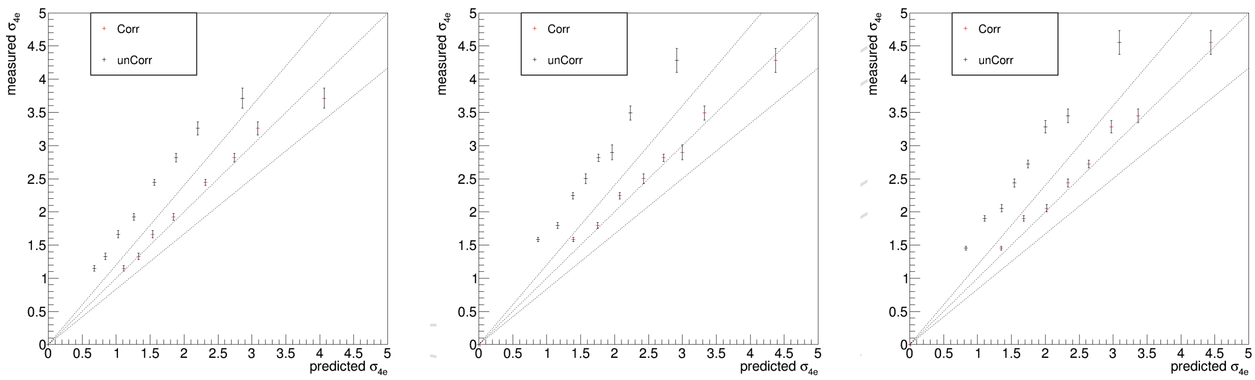

(b) 4e

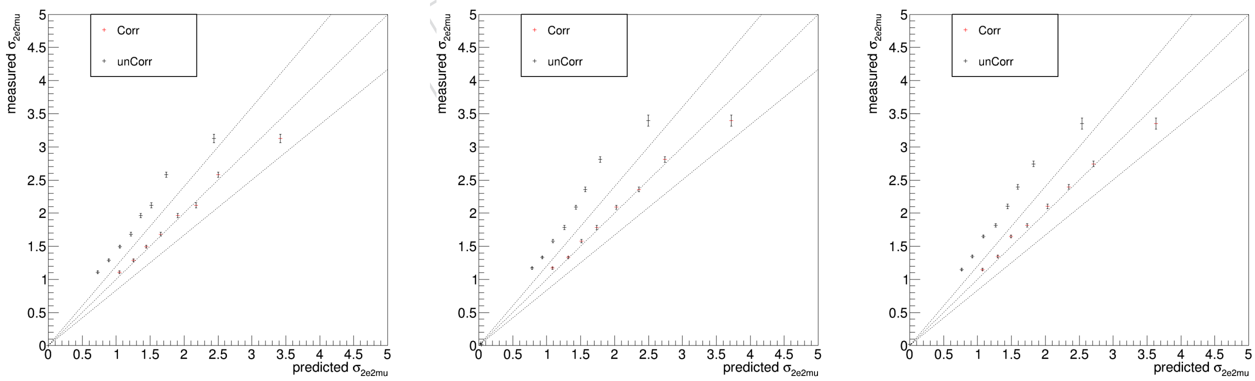

(c) $2e2\mu$

Figure 22: Validation of the per-event mass uncertainties from events in ggF to 4 lepton channel, in MC, for three different final states (4μ on top, 4e in the middle and $2e2\mu$ on bottom), for three years (2016 on the left, 2017 in the middle, 2018 on the right). 20% reference band is also shown.

Expected uncertainty	4μ	4e	$2e2\mu$	$2\mu2e$	inclusive	Stat only
1D model	-	-	-	-	-	-
2D model	-	-	-	-	-	-
relative improvement	-	-	-	-	-	-

Table 6: Higgs boson mass uncertainty measured with 1D and 2D model. All mass values are given in GeV. The uncertainties are the total statistical plus systematic uncertainty, unless otherwise stated.

This offset is called the transverse impact parameter (d_0) and is defined as

$$d_0 \equiv -x_v \sin\phi + y_v \cos\phi, \tag{1}$$

where (x_v, y_v) are the coordinates of the point of closest approach (PCA) along the reconstructed track relative to some reference point (RP), and ϕ is the azimuthal angle in the transverse plane measured relative to the x-axis (Fig. 23, left).

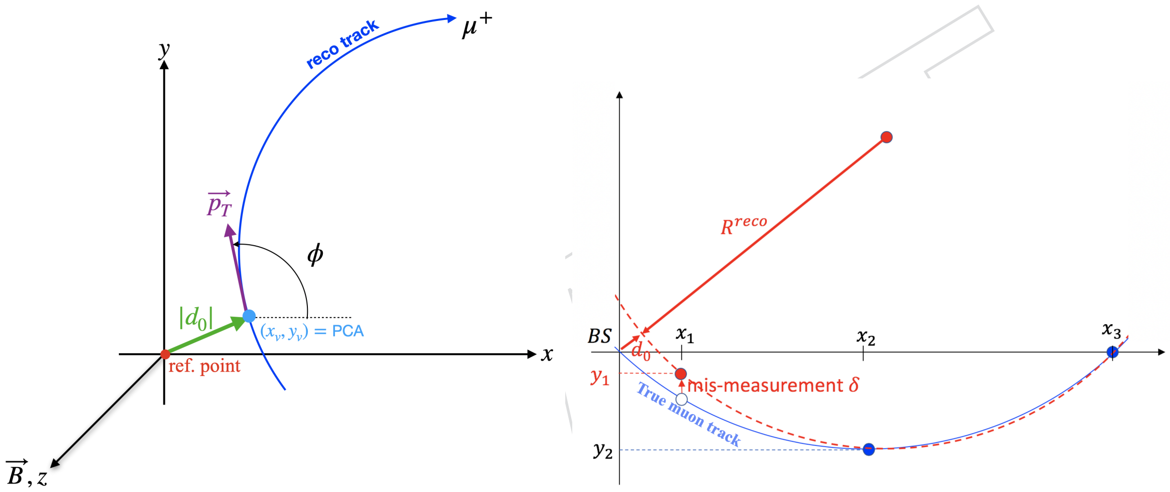

Figure 23: (Left) The coordinates used to define d_0. (Right) A mis-measurement of a hit along a muon track can change the curvature of the track, which in turn affects the measured p_T and d_0.

8.1.1 Beam spot description

This section will describe the beam spot in data and in MC, looking also the stability during run and LHC fill of its position, error and width.

8.1.2 Vertex and beam spot constraint

Section to be filled with results obtained imposing a constraint on the leptons track to a common vertex compatible with the beam spot (in the future, VX+BS).

8.1.3 Ad hoc d_0 corrections

In this study, the RP is taken to be the beam spot (BS).

An imperfectly reconstructed track can yield a d_0 and a shift in the curvature of the track. Changing the track curvature creates a difference between the true p_T and the reconstructed p_T.

This motivates a correlation between d_0 and $p_{\rm T}$ mis-measurement (Fig. 23, Right). Knowledge of such a correlation can allow for muon $p_{\rm T}$ correction and, hence, improved measurement precision such as a decrease in the resolution of $m_{2\mu}$ and $m_{4\mu}$ distributions.
Eqn. 1 shows that the impact parameter is a signed distance. The sign of d_0 is by itself not illuminating; however, taking the product with the muon charge (qd_0) uniquely determines the location of the RP relative to the circular muon trajectory (A.1):

$$\text{RP} = \begin{cases} \text{inside of circle,} & \text{if } qd_0 > 0 \\ \text{outside of circle,} & \text{if } qd_0 < 0. \end{cases}$$

Thus the quantity qd_0 is used in this studies.
Muons from Drell-Yan ($q\bar{q} \to Z/\gamma^* \to 2\mu$) and J/ψ events ($J/\psi \to 2\mu$) were organized into approximately 1800 bins of [$|\eta|$, $p_{\rm T}$, qd_0]. First, muons are split into 13 η bins of approximately equal $\Delta\eta$ within the barrel, overlap, and endcap regions. The bin edges used are:

$$|\eta| : [0.0, 0.2, 0.4, 0.6, 0.8, 1.0, 1.25, 1.5, 1.75, 2.0, 2.1, 2.2, 2.3, 2.4]$$

Next, each $|\eta|$ bin is split into 12 $p_{\rm T}$ bins:

$$p_{\rm T} : [5, 7, 10, 14, 20, 27, 38, 50, 75, 100, 150, 200, 1000] \text{ GeV}.$$

Each [$|\eta|$, $p_{\rm T}$] bin is referred to as a “square”. Finally each square is split into a variable number of qd_0 bins, depending on the number of muons in the square. This 3-D bin of ($|\eta|$, $p_{\rm T}$, qd_0) is referred to as a “cube”. Both of these binning methods allow muons to be approximately evenly divided across ($|\eta|$, $p_{\rm T}$) phase space.

Note on qd_0 binning: The muons in a given square are sorted according to increasing qd_0. Next, the qd_0 bin edges are recorded which divide this set of muons into 12 equal-entry bins. If at least N muons are found in each equal-entry cube, then these are the final 12 qd_0 bin edges for this particular square. If there are fewer than N muons in each cube, the qd_0 axis is instead split into 11 equal-entry bins. Then if N muons are found per cube, the qd_0 bin edges are recorded. Otherwise the procedure is repeated, decreasing the number of equal-entry bins by 1, until either N muons per cube are found or the qd_0 axis is split into a minimum of 2 equal-entry bins. For this analysis N was chosen to be 3000 to ensure sufficient statistics in each cube.

The goal is to check for any correlation between $p_{\rm T}$ mis-measurement and qd_0 in the finely-divided phase space. The $p_{\rm T}$ mis-measurement is defined as

$$p_{\rm T} \text{ mis-measurement} \equiv \frac{p_{\rm T}^{\rm reco} - p_{\rm T}^{\rm gen}}{p_{\rm T}^{\rm gen}} = \Delta p_{\rm T}/p_{\rm T}$$

and a $\Delta p_{\rm T}/p_{\rm T}$ distribution is made for each cube. The Gaussian mean ($\mu_{\rm Gaus}$) of the core of the distribution is extracted using an iterative Gaussian fit technique: this consists in fitting the distribution in a recursive way updating the window fit according to σ and μ of the previous fit. An example of such a distribution and its corresponding fits are shown in Fig. 24. The best-fit $\mu_{\rm Gaus}$ values for each cube are then plotted versus the unbinned average qd_0 of the same cube. The correlation between $\mu_{\rm Gaus}(\Delta p_{\rm T}/p_{\rm T})$ and qd_0 is observed for all ($|\eta|$, $p_{\rm T}$) squares and is approximately linear (Fig. 25). A pair of best-fit parameters (a, b) are extracted from a linear fit for each square:

$$\Delta p_{\rm T}/p_{\rm T} = a + b \cdot \text{avg}(qd_0).$$

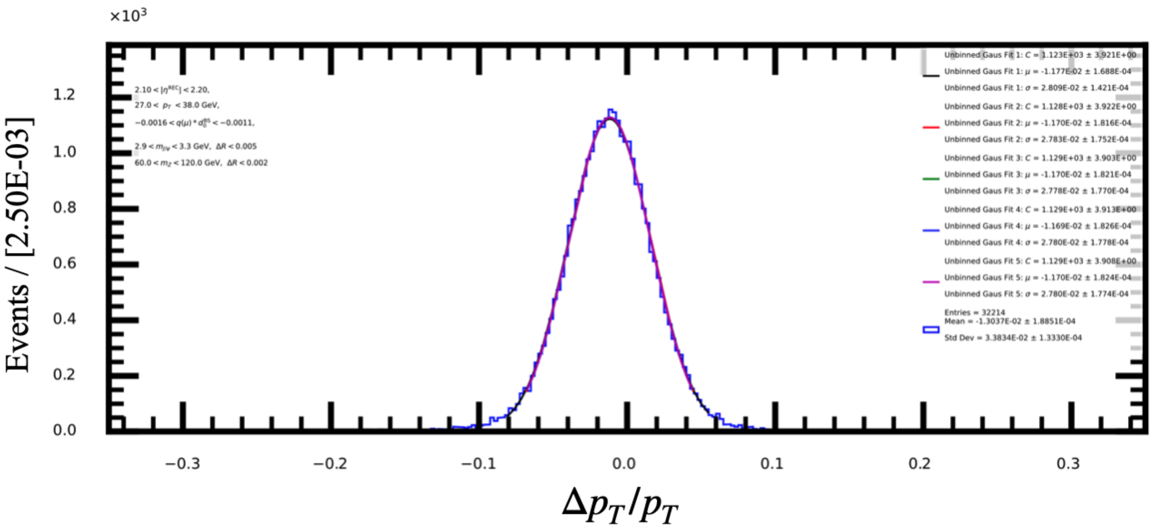

Figure 24: A $\Delta p_\mathrm{T}/p_\mathrm{T}$ distribution made from one of the approximately 1800 "cubes". For this histogram, muons from J/ψ and DY samples pass $2.1 < |\eta| < 2.2$, $27 < p_\mathrm{T} < 38$ GeV, and $-0.0016 < qd_0 < -0.0011$ cm. Iterative Gaussian fits are performed to extract the converged μ_Gaus of the core of the distribution.

The fit parameters can then be used to correct muon p_T based on the kinematical properties of the muon ($|\eta|$, p_T, q, d_0). To obtain the corrected p_T ($p_\mathrm{T}^\mathrm{corr}$), simply shift the reconstructed p_T ($p_\mathrm{T}^\mathrm{reco}$) by the predicted amount:

$$p_\mathrm{T}^\mathrm{corr} = p_\mathrm{T}^\mathrm{reco} - \Delta p_\mathrm{T}.$$

As an example, the best-fit results for $0.0 < |\eta| < 0.2$ and all p_T bins are shown in Fig. 25. The graphs for all $|\eta|$ bins are shown in A.2.

Distributions of $\Delta p_\mathrm{T}/p_\mathrm{T}$, $m_{2\mu}$, and $m_{4\mu}$ were made using 2017 and 2018 MC samples before any p_T corrections were applied. Then p_T corrections were applied on a per muon basis and the distributions were remade. Details of the fits of each distribution and the improvement of σ from each distribution were as follows:

- **$\Delta p_\mathrm{T}/p_\mathrm{T}$ distributions:**
  Muons from J/ψ and DY samples were sorted into all 156 ($|\eta|$, p_T) squares and $\Delta p_\mathrm{T}/p_\mathrm{T}$ distributions were made in each. Six iterative Gaussian fits were performed per square to extract the best-fit σ_Gaus before and after p_T correction. Fig. 26 shows examples of two such distributions and fits for 2018 MC. Improvements in the σ_Gaus for all squares for 2017 and 2018 MC are shown in Fig 27.
- **$\mathrm{m}_{2\mu}$ distributions:**
  DY events with $60 < \mathrm{m}_{2\mu} < 120$ GeV were used to form $\mathrm{m}_{2\mu}$ distributions for 2017 and 2018 MC. A Breit-Wigner function convoluted with a Crystal Ball (CB) function is used to fit the $\mathrm{m}_{2\mu}$ signal line shape while an exponential function is added to describe the interferring non-resonant background. The fit is performed on a binned distribution and the σ_CB is extracted. The p_T of the muons is corrected and the distribution is refit to get $\sigma_\mathrm{CB}^\mathrm{corr}$. The improvement in σ_CB is 4.6% for 2017 (Fig. 28, left) and 7.6% for 2018 (Fig. 28, right).
- **$\mathrm{m}_{4\mu}$ distributions:**
  Distributions of $\mathrm{m}_{4\mu}$ are made using 2017 and 2018 gluon-gluon fusion (ggH) MC samples. Events were required to pass $105 < \mathrm{m}_{4\mu} < 140$ GeV. An unbinned DSCB fit

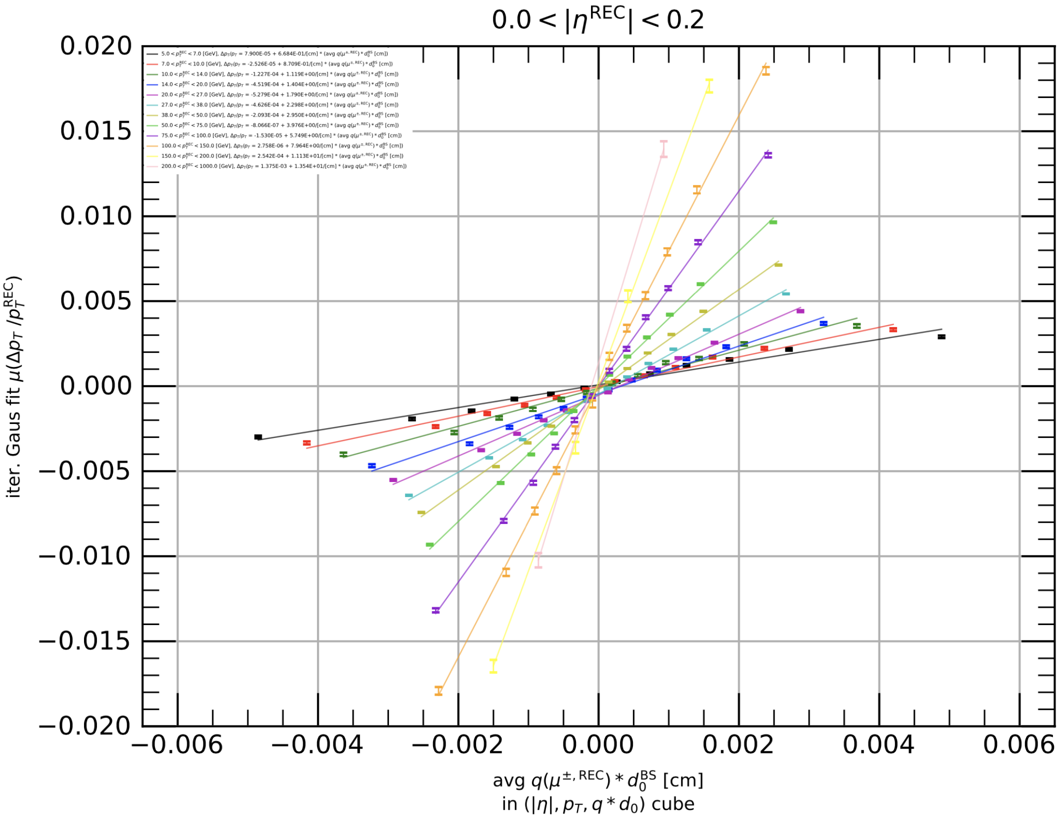

Figure 25: A graph of $\mu_{\mathrm{Gaus}}(\Delta p_{\mathrm{T}}/p_{\mathrm{T}})$ vs. avg(qd_0) in a single $|\eta|$ bin $(0.0 < |\eta| < 0.2)$ for 2018 MC. Each line uses data from a single p_{T} bin. The best-fit parameters are shown in the legend and used to correct muon p_{T}.

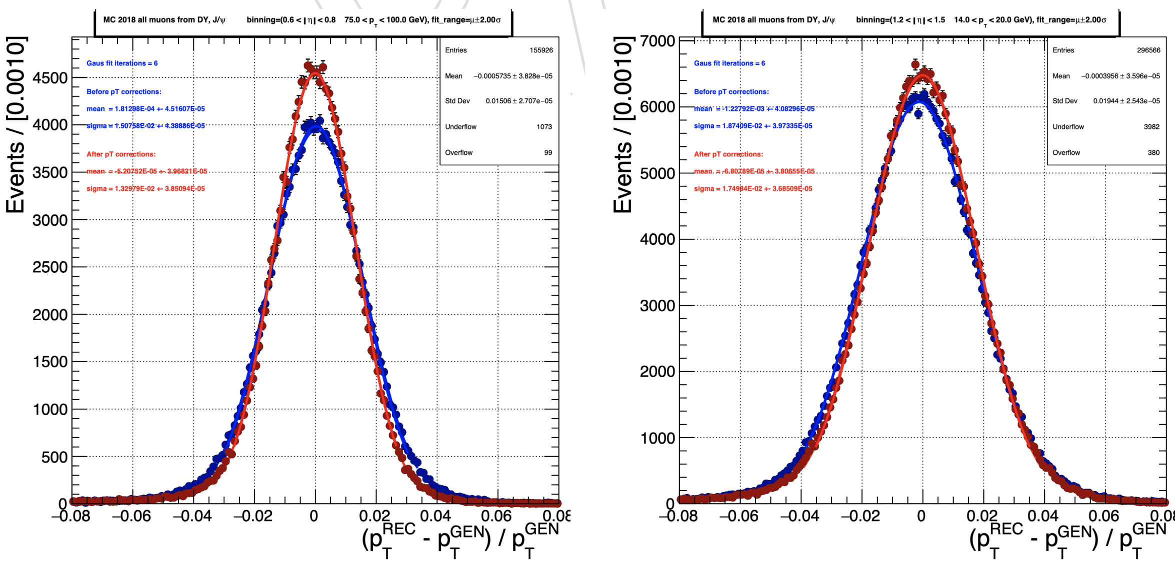

Figure 26: A $\Delta p_{\mathrm{T}}/p_{\mathrm{T}}$ distribution is made for each of the 156 $(|\eta|,\ p_{\mathrm{T}})$ squares using muons before (blue) and after (red) p_{T} corrections. The two example plots shown here use muons from 2018 samples and show σ_{Gaus} improvements of 11.8% in a narrow section of the barrel (left) and overlap/endcap (right).

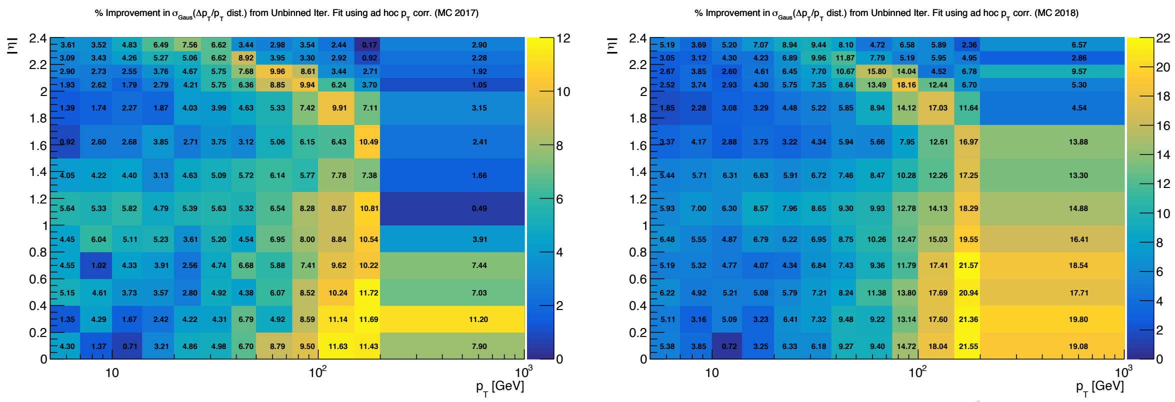

Figure 27: Tables showing the percent improvement in iterated Gaus. fit σ_{Gaus} $(\Delta p_{\mathrm{T}}/p_{\mathrm{T}})$ for each $(|\eta|, p_{\mathrm{T}})$ square by applying ad hoc p_{T} corrections to muons from DY and J/ψ samples for 2017 (left) and 2018 (right) MC.

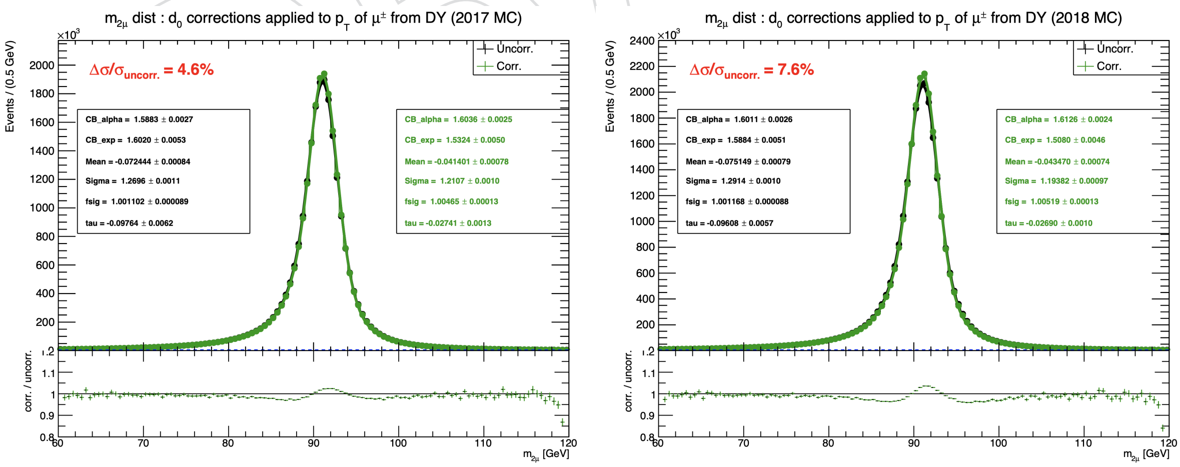

Figure 28: Distributions of $m_{2\mu}$ before (black line) and after (green line) muon p_{T} correction.

was performed on the $m_{4\mu}$ distribution and the σ_{DSCB} was extracted. After correcting muon p_{T}, remaking, and refitting the distributions, a 4.3% improvement in σ_{DSCB} was obtained for 2017 MC (Fig. 29, left) and 6.1% improvement for 2018 MC (Fig. 29, right).

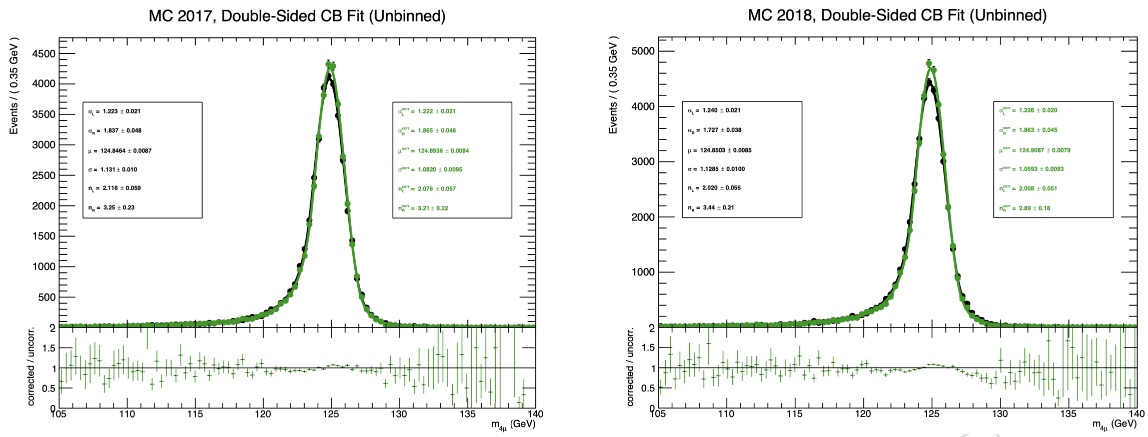

Figure 29: Distributions of $m_{4\mu}$ before (black line) and after (green line) muon p_{T} correction.

8.1.4 Toy model study

This section will describe the theoretical improvement that can be gained, with a constraint to the beam spot, during muon reconstruction.

8.1.5 Refitted pT with constraint

Section to be filled.

8.1.6 Validation

Section to be filled.

8.1.7 Expected mH measurement uncertainties and relative improvements

This section will describe how the mass uncertainty will improve with new muon reconstruction.

The new four-lepton mass ($m_{4\ell}^{VX+BS}$) and the new mass error uncertainty ($D_{m_{4\ell}}^{VX+BS}$) are used to rebuilt the 2D likelihood function, $\mathcal{L}(m_{4\ell}^{VX+BS}, D_{m_{4\ell}}^{VX+BS}|m_H)$. The expected m_{H} measurement uncertainty, in case of no-bkg and no-syst, split for different final state, is reported in Table 7, compared with 1D result.

Expected uncertainty	4μ	4e	$2e2\mu$	$2\mu2e$	inclusive	Stat only
2D model with muon refit	-	-	-	-	-	-
2D model	-	-	-	-	-	-
relative improvement	-	-	-	-	-	-

Table 7: Higgs boson mass uncertainty measured with 2D model, with and without new muon reconstruction. All mass values are given in GeV. The uncertainties are the total statistical plus systematic uncertainty, unless otherwise stated.

8.2 Refitting muon and electron pT with a Z1-mass constraint

8.2.1 Z1-mass line shape

In order to improve the four lepton invariant mass resolution, a kinematic fit is also performed using a mass constraint on the intermediate on-shell Z resonance, using an approach similar to the one described in [8]. The basic idea is to re-evaluate p_T of two leptons forming the Z bosons of the Higgs candidate, with a constraint on the reconstructed Z mass to follow the Z boson true lineshape. For a 125 GeV Higgs, the selected Z_1 is mostly on-shell, while m_{Z_2} distribution is broad and the spread is much bigger than detector resolution. When considering mass measurment of 125 GeV Higgs, expected gain in resolution comes from refitting Z_1. The likelihood to be maximized can be written as:

$$\mathcal{L}(p_T^1, p_T^2 | p_T^{reco1}, \sigma p_T^1, p_T^{reco2}, \sigma p_T^2) = Gauss(p_T^{reco1} | p_T^1, \sigma p_T^1) \cdot Gauss(p_T^{reco2} | p_T^2, \sigma p_T^2) \cdot \mathcal{L}(m_{12} | m_Z, m_H)$$

where $p_T^{reco1,2}$ are the reconstructed transverse momentum of the two leptons forming the Z_1, $\sigma_{p_T^{1,2}}$ are the per lepton resolution (uncertainty on p_T measurement, corrected using method described in 7.1), $p_T^{1,2}$ are the observables under optimisation, m_{12} is the invariant mass calculated from p_T^1 and p_T^2. $\mathcal{L}(m_{12}|m_Z, m_H)$ is the likelihood, given the true lineshape of m_{Z_1}.
For each event, the likelihood is maximized and p_T information of the refitted leptons are updated. A comparison between measured $\sigma_{m_{4\ell}}$ and prediction after refitting, following same procedure as described in 7.1.3, is performed. Figure 30 shows the closure test after refitting procedure.

8.2.2 Refitted pT with constraints

This section will be filled with the description of the Z1 constraint procedure in case of new muon reconstruction.

8.2.3 Validation

Section to be filled.

8.3 Expected mH measurement uncertainties (MC) and relative improvements

The new four-lepton mass ($m'_{4\ell}$) and the new mass error uncertainty (D'_m), obtained after the constraint of the on-shell Z boson, are used to rebuilt the 2D likelihood function, $\mathcal{L}(m'_{4\ell}, D'_m)|m_H)$.
The expected m_H measurement uncertainty, in case of no-bkg and no-syst, split for different final state, is reported in Table 8, compared with 2D result.

Expected uncertainty	4μ	4e	$2e2\mu$	$2\mu 2e$	inclusive	Stat only
2D model with Z1 constraint	-	-	-	-	-	-
2D model	-	-	-	-	-	-
relative improvement	-	-	-	-	-	-

Table 8: Higgs boson mass uncertainty measured with 2D model, with and without the Z1 constraint. All mass values are given in GeV. The uncertainties are the total statistical plus systematic uncertainty, unless otherwise stated.

Next step will be to taken into account also the new muon reconstruction. Final 2D model ($\mathcal{L}(m'^{VX+BS}_{4\ell}, D'^{VX+BS}_m|m_H)$) results are shown in Table 9, compared with previous result.

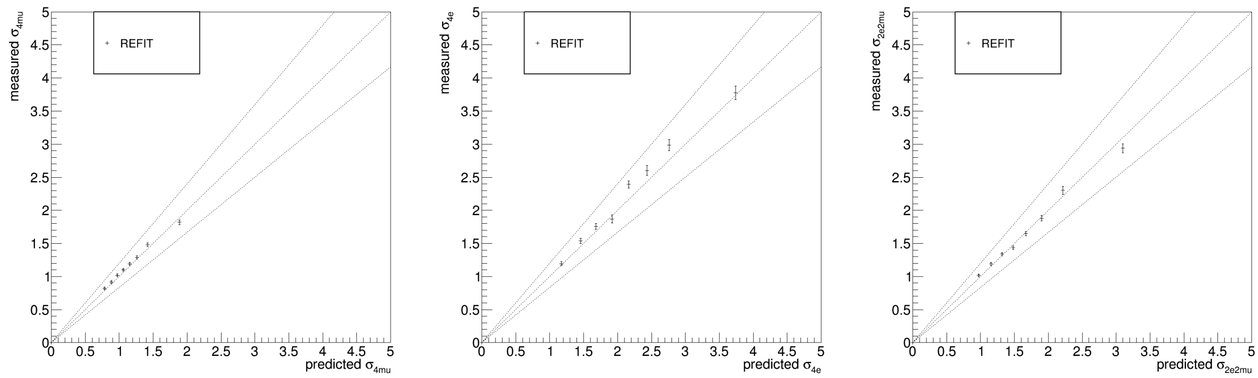

(a) 2016

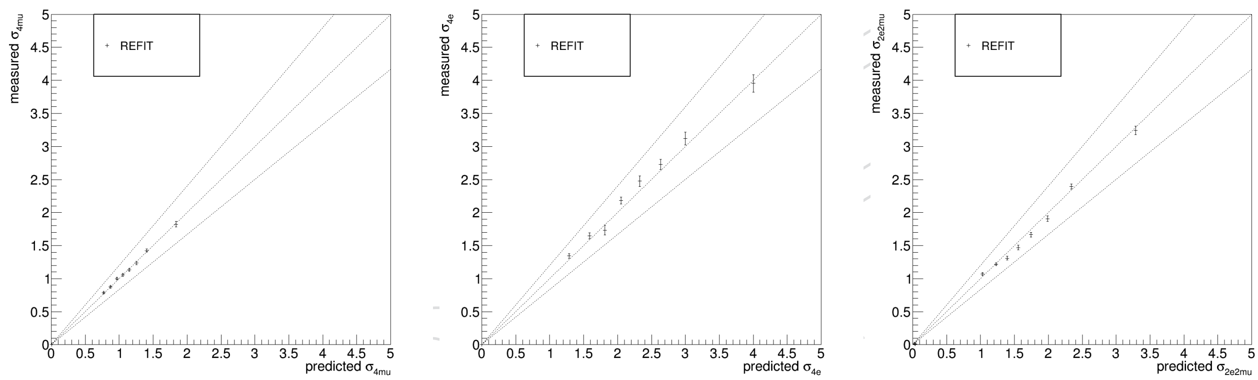

(b) 2017

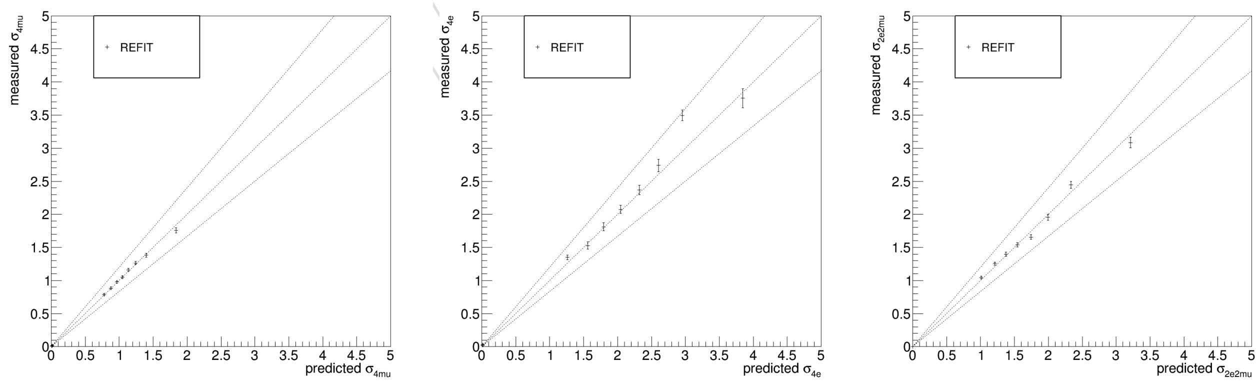

(c) 2018

Figure 30: Closure test after Z_1 constraint, for different final states of m_H = 125GeV MC sample. 4μ on the left, 4e in the middle and $2e2\mu$ on the right.

Expected uncertainty	4μ	4e	$2e2\mu$	$2\mu 2e$	inclusive	Stat only
2D model (with Z1 and muon refit)	-	-	-	-	-	-
2D model (with Z1)	-	-	-	-	-	-
relative improvement	-	-	-	-	-	-

Table 9: Higgs boson mass uncertainty measured with 2D model, with and without the new muon reconstruction. All mass values are given in GeV. The uncertainties are the total statistical plus systematic uncertainty, unless otherwise stated.

9 Matrix Element-based Kinematic Discriminant (D^{kin}_{bkg})

The D^{kin}_{bkg} is the third variable that is used to extract Higgs boson mass result. It is a discriminant sensitive to $gg/q\bar{q} \rightarrow 4\ell$ kinematics: more info in [6].

9.1 D^{kin}_{bkg} with new muon reconstruction

This section will show the possible impact of the new muon reconstruction on the D^{kin}_{bkg}.

10 Background Estimation

10.1 Irreducible background

10.1.1 ggZZ background

Following prescription of [6], the $gg \rightarrow ZZ$ background is re-weighted with a k factor to reach NNLO precision.

10.1.2 qqZZ background

The $qq \rightarrow ZZ$ background is generated at NLO and then scaled to NNLO with a NNLO/NLO k-factors, as a function of m(ZZ). Additional NLO electroweak corrections which depend on the initial state quark flavor and kinematics are also applied to this process in the region $m(ZZ) > 2m(Z)$, where the corrections have been computed. For more detalis and plots, see [6].

10.2 Reducible background

10.2.1 General Methodology

The reducible background contribution, hereafter called Z+X, is currently obtained, for 2017 and 2018, scaling according to the luminosity the shape of the Z+X contribution evaluated in [5] for 2016.
This background will evaluated properly, following next steps.

10.2.2 Tight-to-loose lepton rates

10.2.3 3P1F and 2P2F control regions

10.2.4 Predictions

10.2.5 Validation using wrong-flavour-wrong-charge control sample

11 Yields and distributions

11.1 Yields

The number of observed events together with the expected yields for signal and background, after the full selection, are reported in Table 10, for the mass range of interest, $105 < m_{4\ell} < 140$ GeV.

channel	4μ	4e	$2e2\mu$+$2\mu2e$	inclusive
qqZZ	-	-	-	223.79
ggZZ	-	-	-	22.50
Z+X	-	-	-	136.84
Sum of background	-	-	-	383.13
Signal (m_H = 125 GeV)	-	-	-	243.38
Total expected	-	-	-	626.51
Observed	-	-	-	-

Table 10: Yields.

11.2 Distributions

The distributions of 4-lepton mass, 4-lepton mass error and D_{bkg}^{kin} are shown in Figure 31, for the inclusive final state, combining all channels.

12 Expected m_{H} uncertainties using a 3D pdf

12.1 3D model: $\mathcal{L}(m_{4\ell}, D_{m_{4\ell}}, D_{bkg}^{kin})$

This section will described the three-dimentional likelihood function built with the 4-lepton mass, the mass uncertainty and the kinematical discriminant considering the new muon reconstruction and the Z1 constraint: $\mathcal{L}(m_{4\ell}'^{VX+BS}, D_{m_{4\ell}}'^{VX+BS}, D_{bkg}^{kin}|m_H)$. The backgrounds described in 10 are considered (gg and $q\bar{q}$ and the Z+jets). Expected results (in GeV) are summarised in Table 11.

Expected uncertainty	4μ	4e	$2e2\mu$	$2\mu2e$	inclusive	Stat only
3D model (with Z1 and muon refit)	-	-	-	-	-	-
2D model (with Z1 and muon refit)	-	-	-	-	-	-
relative improvement	-	-	-	-	-	-

Table 11: Best fit values for the mass of the Higgs boson measured in the 4ℓ final states, with 3D model. All values are given in GeV. The uncertainties are the total statistical plus systematic uncertainty.

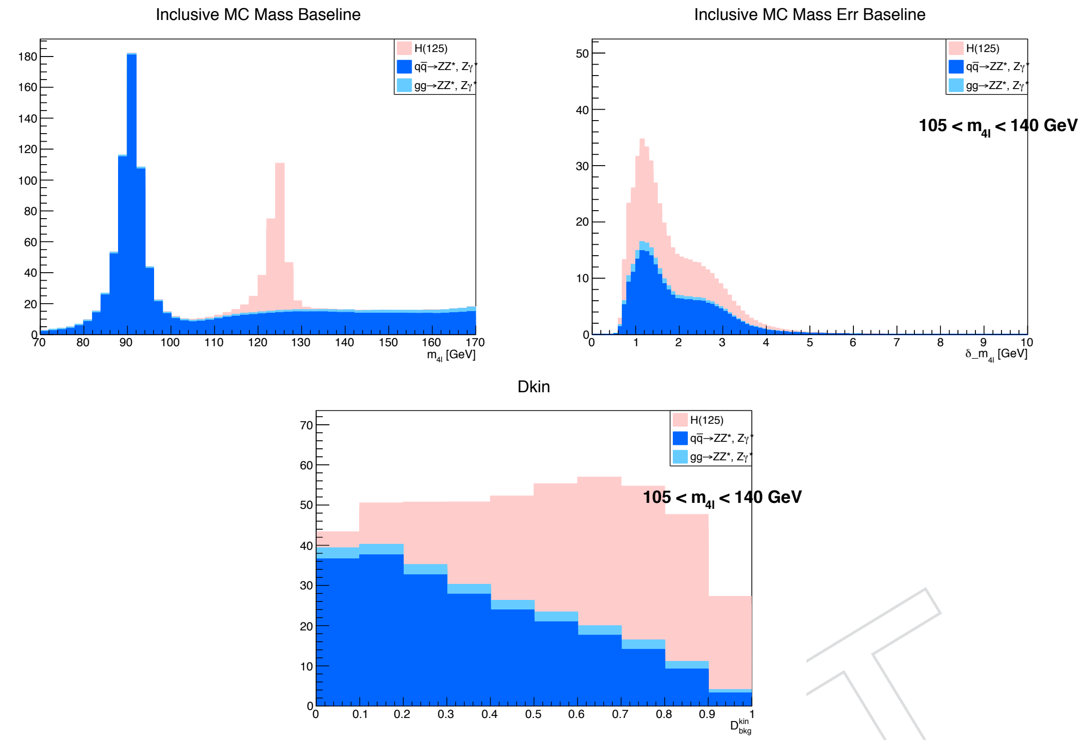

Figure 31: Distribution of 4-lepton mass, 4-lepton mass error and D^{kin}_{bkg}, combining all final states and all years.

12.2 Correlation studies

This section will describe the studies about possible correlation building the 3D model.

13 Systematic uncertainties

The systematic uncertainties, taken into account to derive final results, are currently the same for all three years and their estimation is based on [5]. Only lepton momentum scale has been re-estimated for each year and it has been updated.
Systematic will be evaluated properly.

13.1 Uncertainty on lepton momentum scale and resolution

Uncertainty in the lepton energy scale is the dominant source of systematic uncertainty in Higgs mass measurement.
For muons, after applying the Rochester correction, it is important to evaluate the residual disagreement between data and simulation (non-closure uncertainty). Same for eletrons, where the non-closure uncertainty needs to be measured, after applying the scale-smearing correction.
Non-closure uncertainty in the Higgs boson mass measurement is determined by considering the $Z \to \ell\ell$ mass distributions in data and simulation. Events are separated into categories based on the p_T and η of one of the two leptons, and integrating over the other. The dilepton mass distributions are then fit with a BW convoluted with a DSCB function. The offsets in the measured peak position with respect to the nominal Z boson mass in data and simulation are extracted, and the results are shown in Figure 32.

For the non-closure uncertainty, this offset (called x) is propagated to each lepton, in simulated Higgs events, according its p_{T} - η bin: $p_{\mathrm{T}}^{new^{\pm}} = p_{\mathrm{T}}^{old} * (1 \pm x)$. Then, the $m_{4\ell}$ is recalculated three times: nominal, scale up (considering $p_T^{new^+}$), scale down ($p_T^{new^-}$). Finally the no-closure uncertainty for $m_{4\ell}$ is determined by comparing fitted mass mean $m_{4\ell}^{nominal}$ with $m_{4\ell}^{scaleup}$ and $m_{4\ell}^{scaledown}$, for each final state. The non-closure uncertainty is determined to be 0.02%, 0.08% across three years for the 4μ, 4e, respectively.
Same procedure is used to propagate the uncertainties of the corrections in the electron case, using as offset the uncertainties provided by the eGamma POG. The uncertainty caused by scale-smearing correction is determined to be 0.4%, 0.7% and 0.3% for three years. These are summed in quadrature to the previous ones, obtaining 0.01% for 2016 and 2018 while 0.015% for 2017. For muon, uncertainty is 0.02% for all three years.

The uncertainty in the 4-lepton mass resolution coming from the uncertainty in the per-lepton energy resolution is 20%, as described in [5].

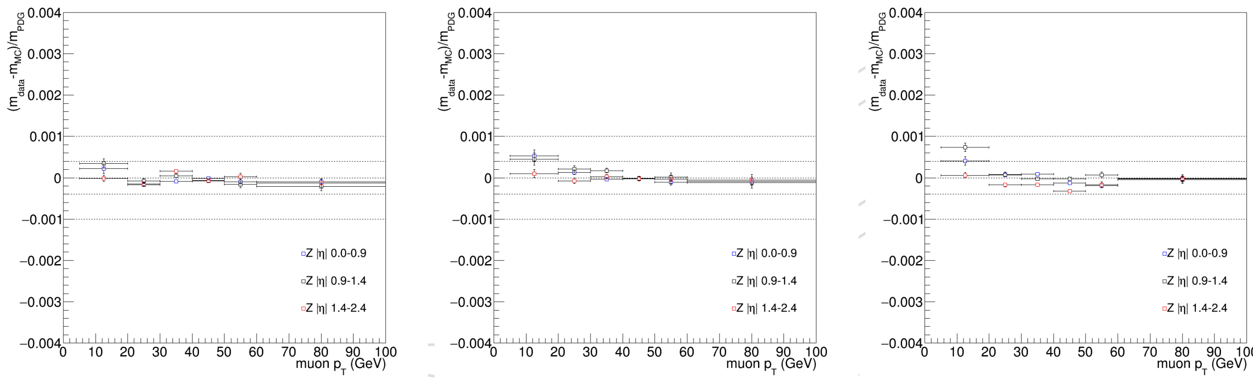

(a) muon

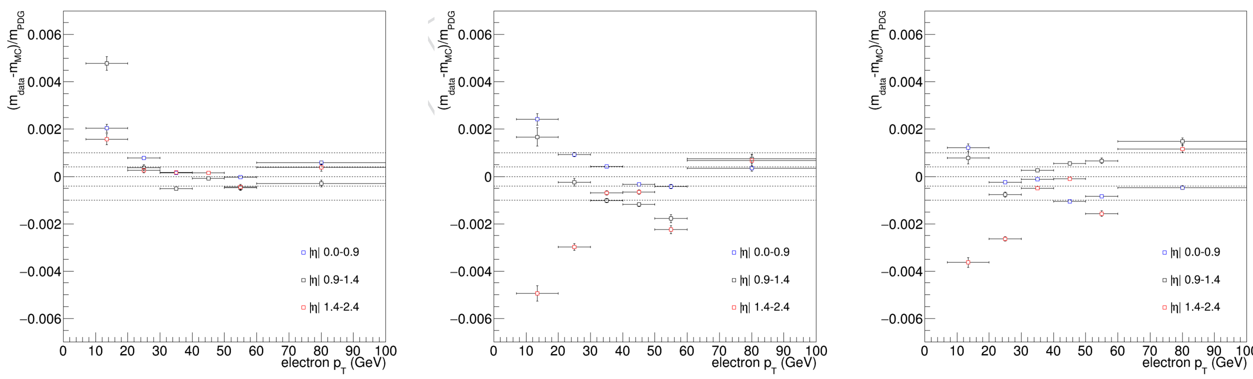

(b) electron

Figure 32: Lepton scale non-closure uncertianty for muons (top) and electrons (bottom): 2016 on the left, 2017 in the middle and 2018 on the right.

13.2 Lepton efficiency

The uncertainty on the lepton identification and reconstruction efficiency ranges from 2.5-9%, depending on the final state considered.

13.3 Theory cross section

Theoretical uncertainties which affect both signal and background estimation include uncertainties from the renormalization and factorization scale and choice of PDF set. An additional uncertainty of the 10% on the K factor used for the gg $\rightarrow$ ZZ $\rightarrow 4\ell$ prediction is applied. Table 12 summarises the systematic uncertainties used.

A systematic uncertainty of 2% on the branching ratio of H $\rightarrow$ ZZ* $\rightarrow 4\ell$ only affects the signal

Theory uncertainties			
Name	2016	2017	2018
QCD scale ggH	±3.9%		
QCD scale VBF	+0.4/-0.3%		
QCD scale WH	+0.5/-0.7%		
QCD scale ZH	+3.8/-3.1%		
QCD scale ttH	+5.8/-9.2%		
QCD scale ttH	+5.8/-9.2%		
QCD scale qqZZ	+3.2/-4.2%		
QCD scale ggZZ	±3.9%		
PDF set gg	±3.2%		
PDF set qq	±2.1%		

Table 12: Summary of the systematic uncertainties.

yield is also considered.

13.4 Luminosity

The uncertainty on the integrated luminosity affects both signal and background. For the current results, this uncertainty is 2.6% for all three years.

13.5 Data-driven samples

Experimental uncertainties for the reducible background estimation, described in Section 10.2, vary between 36% (4μ) and 43% (4e).

14 Higgs mass measurement results

14.1 Final Results

Final results, including the systematic uncertainties described in 13 are summarised in Table 13. **These results are currently obtained using standard muon reconstruction - e.g. no vertex constraint neither ad-hoc correction.**

14.2 Dominant systematics

Section to be filled.

14.3 Comparison with older CMS and ATLAS results

Section partially filled.

The comparison of the newest results and the previous ones from CMS [5] is shown in Table 14.

Expected uncertainty	4μ	4e	$2e2\mu$	$2\mu 2e$	inclusive	(Stat only)
3D model + refit	-	-	-	-	-0.128/+0.127	-0.12/+0.12
3D model	-	-	-	-	-0.136/+0.135	-0.129/+0.130
2D model	-	-	-	-	-0.142/+0.141	-0.135/+0.136
1D model	-	-	-	-	-0.161/+0.159	-0.155/+0.155

Table 13: Best fit values for the mass of the Higgs boson measured in the 4ℓ finalstates, with 3D model, with (top row) and without (bottom row) Z_1 constraint. All mass values are given in GeV. The uncertainties are the total statistical plus systematic uncertainty.

Expected uncertainty	HIG-16-041	New
3D model + refit	-0.257/+0.255	-0.128/+0.127
3D model	-0.279/+0.278	-0.136/+0.135
2D model	-0.289/+0.287	-0.142/+0.141
1D model	-0.324/+0.321	-0.161/+0.159

Table 14: Best fit values for the mass of the Higgs boson measured in the 4ℓ final states, with 3D model, with (top row) and without (bottom row) Z_1 constraint. All mass values are given in GeV. The uncertainties are the total statistical plus systematic uncertainty.

14.4 Validation using $4l$ decays

Section to be filled.

15 Higgs on-shell width measurement results

Preliminary results are under investigations.

15.1 Dominant systematics

15.2 Comparison with older CMS and ATLAS results

Previous expected CMS results (at 68% C.L.) was $\Gamma_H < 0.750$ GeV

16 Conclusions

Higgs boson mass and on-shell width measurements have been presented. The analysis has been performed using Full Run 2 data collected by the CMS detector at LHC during 2016-2018, at a center-of-mass energy of 13 TeV, corresponding to an integrated luminosity of 137 fb^{-1}. Final expected results are: $m_H = 125^{+0.127}_{-0.128}$ $[^{+0.12}_{-0.12}(\text{stat})]$ GeV and $\Gamma_H = XXX$ GeV.

References

[1] G. Aad and A. Schaelicke, "Observation of a new particle in the search for the standard model higgs boson with the atlas detector at the lhc", *Phys.Lett.* **B716** (09, 2012) 1–29.

[2] CMS Collaboration Collaboration, "A measurement of the Higgs boson mass in the diphoton decay channel", *Phys. Lett. B* **805** (Feb, 2020) 135425. 37 p, `doi:10.1016/j.physletb.2020.135425`. Replaced with the published version. Added the journal reference and the DOI. All the figures and tables can be found at http://cms-results.web.cern.ch/cms-results/public-results/publications/HIG-19-004 (CMS Public Pages).

[3] ATLAS Collaboration Collaboration, "Measurement of the Higgs boson mass in the $H \to ZZ^* \to 4\ell$ decay channel with $\sqrt{s} = 13$ TeV pp collisions using the ATLAS detector at the LHC",.

[4] CMS Collaboration Collaboration, "Measurements of the higgs boson width and anomalous hvv couplings from on-shell and off-shell production in the four-lepton final state", *Phys. Rev. D* **99** (Jun, 2019) 112003, `doi:10.1103/PhysRevD.99.112003`.

[5] CMS Collaboration Collaboration, " Measurements of properties of the Higgs boson decaying into four leptons in pp collisions at sqrts = 13 TeV",.

[6] `http://cms.cern.ch/iCMS/analysisadmin/cadilines?line=HIG-19-001&tp=an&id=2200&ancode=HIG-19-001`.

[7] Particle Data Group Collaboration, "Review of particle physics", *Phys. Rev. D* **98** (Aug, 2018) 030001, `doi:10.1103/PhysRevD.98.030001`.

[8] M. A. et al, "Higgs measurements in the channel using kinematic1308fitting technique", *CMS AN2015/285* (2015).

A Ad hoc d_0 studies

A.1 The sign of qd_0

Consider a reconstructed muon track projected onto the xy plane, transverse to the beam pipe. If the muon was a prompt muon, then it truly originated from the primary vertex (PV). However, due to inefficiencies in reconstructing the muon track, the best-fit track may not intersect the PV.

Looking at Figure 33 (Left), the (very exaggerated) muon track is represented by the black circle. This track could either be a μ^+ (blue arrowheads) travelling around clockwise, since the magnetic field points along the $+\hat{z}$ direction, or it could represent the track of a μ^- (orange arrowheads) travelling anticlockwise.

It is convenient to define a few variables:

- $\vec{s}$ = the field point vector which begins at the PV (the origin) and ends at the point-of-closest-approach (PCA) along the muon track.
- ϕ_s = the azimuthal angle of $\vec{s}$ as measured from the x-axis.
- $\phi_{\mu^\pm}$ = the azimuthal angle of the $\vec{p}_{T,\mu^\pm}$, tangent to the track at the PCA, measured from the x-axis.

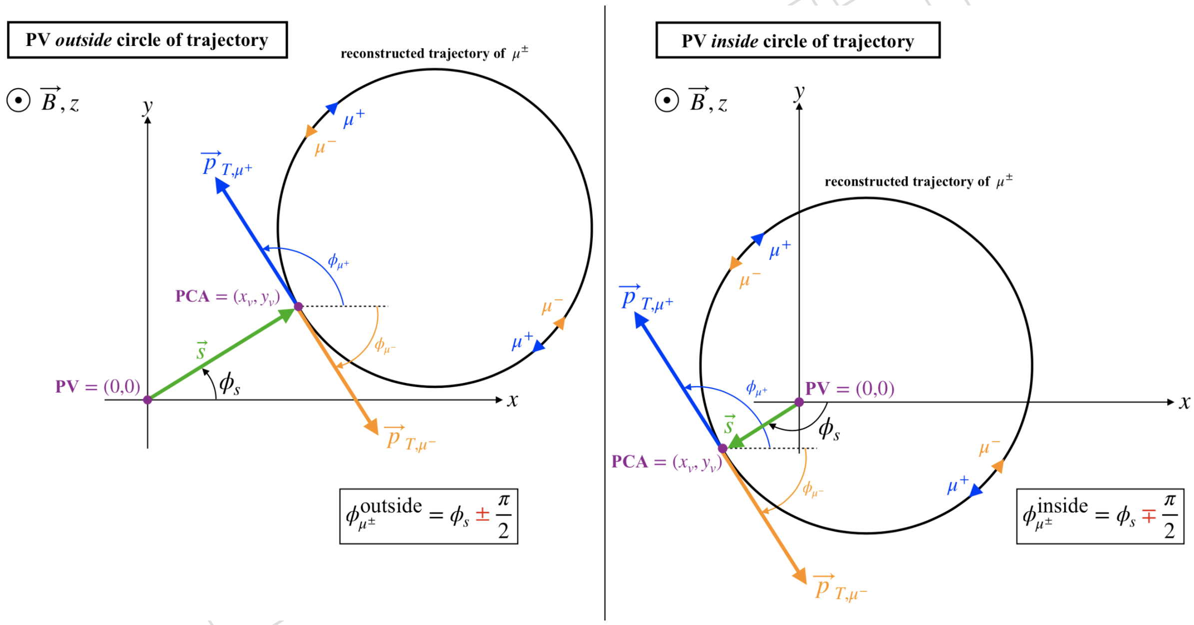

Figure 33: (Left) The case in which the true primary vertex (PV) is *outside* the circular trajectory of a muon. (Right) The opposite case in which the PV is *inside* the circular trajectory.

From Fig. 33 (Left) we see that:

$$\phi_{\mu^\pm} = \phi_s \pm \pi/2. \tag{2}$$

Using one possible definition of d_0 and Equation 2 shows that the d_0 for $\mu^\pm$ which came from a

PV outside the circle trajectory is:

$$\begin{aligned}
d_{0,\mu^\pm}^{\text{PV,outside}} &= -x\sin(\phi_{\mu^\pm}) + y\cos(\phi_{\mu^\pm}) \\
&= -x\sin(\phi_s \pm \pi/2) + y\cos(\phi_s \pm \pi/2) \\
&= -x\big[\sin(\phi_s)\cos(\pi/2) \pm \sin(\pi/2)\cos(\phi_s)\big] + y\big[\cos(\phi_s)\cos(\pi/2) \mp \sin(\phi_s)\sin(\pi/2)\big] \\
&= -x[\pm\cos(\phi_s)] + y[\mp\sin(\phi_s)] \\
&= \mp[x\cos(\phi_s) + y\sin(\phi_s)] \\
&= \mp\big[x\hat{x} + y\hat{y}\big]\cdot\big[\cos(\phi_s)\hat{x} + \sin(\phi_s)\hat{y}\big] \\
&= \mp\vec{s}\cdot\hat{s} \\
&= \mp|\vec{s}||\hat{s}|\cos(0)
\end{aligned}$$

$$\implies d_{0,\mu^\pm}^{\text{PV,outside}} = \mp|\vec{s}|. \tag{3}$$

The case for the PV being *inside* the circle trajectory (Fig. 33, Right) simply leads to a sign change in Eqn. 2:

$$\phi_{\mu^\pm} = \phi_s \mp \pi/2. \tag{4}$$

Starting again from the definition of d_0, but this time using Eqn. 4, ultimately gives:

$$\implies d_{0,\mu^\pm}^{\text{PV,inside}} = \pm|\vec{s}|. \tag{5}$$

Indeed we see that the magnitude of d_0 *is the transverse impact parameter* ($|\vec{s}|$), as expected! The sign of d_0, however, is not possible to interpret at this point: for a $d_0 > 0$ could either mean a μ^- coming from a PV outside the circlular trajectory *or* could mean a μ^+ coming from a PV found inside the circle.

Since the sign of d_0 is not useful by itself, consider multiplying d_0 by the charge of its corresponding muon. We then see that Eqn. 3 becomes:

$$\begin{aligned}
\text{charge}(\mu^\pm)\cdot d_{0,\mu^\pm}^{\text{PV,outside}} &= \pm 1\cdot\mp|\vec{s}| \\
&= -|\vec{s}| < 0,
\end{aligned}$$

which is always negative. Similarly, Eqn. 5 gives the opposite result:

$$\text{charge}(\mu^\pm)\cdot d_{0,\mu^\pm}^{\text{PV,inside}} = +|\vec{s}| > 0,$$

which of course is always positive.

Therefore, if we know the sign of the muon (say, negative) and the sign of its d_0 (say, positive), then we can simply take the product (negative in this case) and infer that the PV must have been *outside* the muon trajectory!

To summarize: it is the *product* of the charge and d_0 that contains useful information about the muon track.

$$\text{PV} = \begin{cases} \text{inside of circle}, & \text{if charge}(\mu^\pm)\cdot d_{0,\mu^\pm} > 0 \\ \text{outside of circle}, & \text{if charge}(\mu^\pm)\cdot d_{0,\mu^\pm} < 0. \end{cases}$$

A.2 Correlation between p_T bias and qd_0

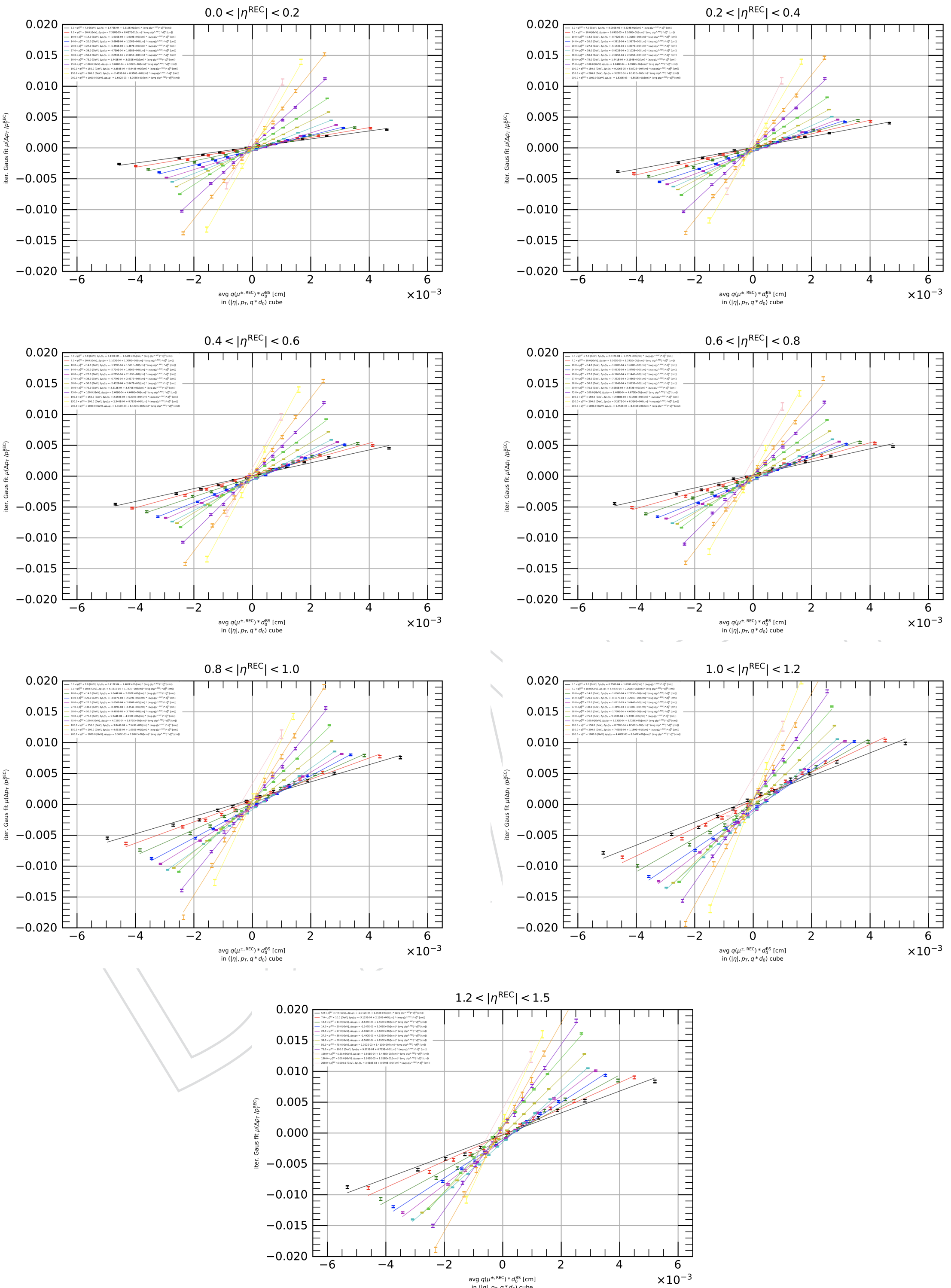

Figure 34: Graphs of $\Delta p_T / p_T$ vs. avg(qd_0) for each $|\eta|$ bin using 2017 MC. The $|\eta|$ bin edges shown above are: $[0.0, 0.2, 0.4, 0.6, 0.8, 1.0, 1.25, 1.5]$. Each line uses data from a single p_T bin. The p_T correction parameters for each ($|\eta|$, p_T) bin are found in the legend.

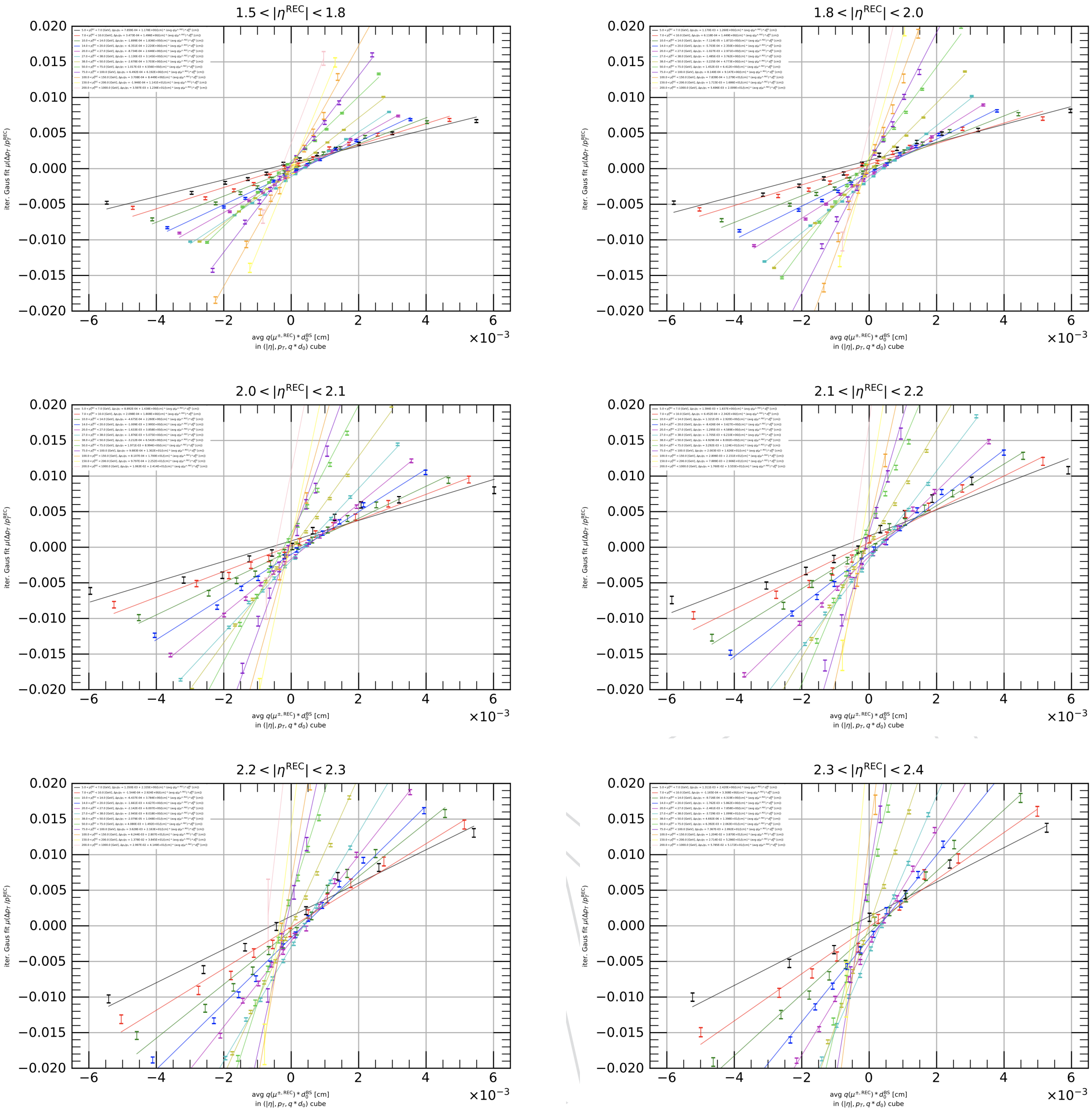

Figure 35: Graphs of $\Delta p_{\mathrm{T}}/p_{\mathrm{T}}$ vs. $\mathrm{avg}(qd_0)$ for each $|\eta|$ bin using 2017 MC. The $|\eta|$ bin edges shown above are: $[1.5, 1.75, 2.0, 2.1, 2.2, 2.3, 2.4]$. Each line uses data from a single p_{T} bin. The p_{T} correction parameters for each ($|\eta|$, p_{T}) bin are found in the legend.

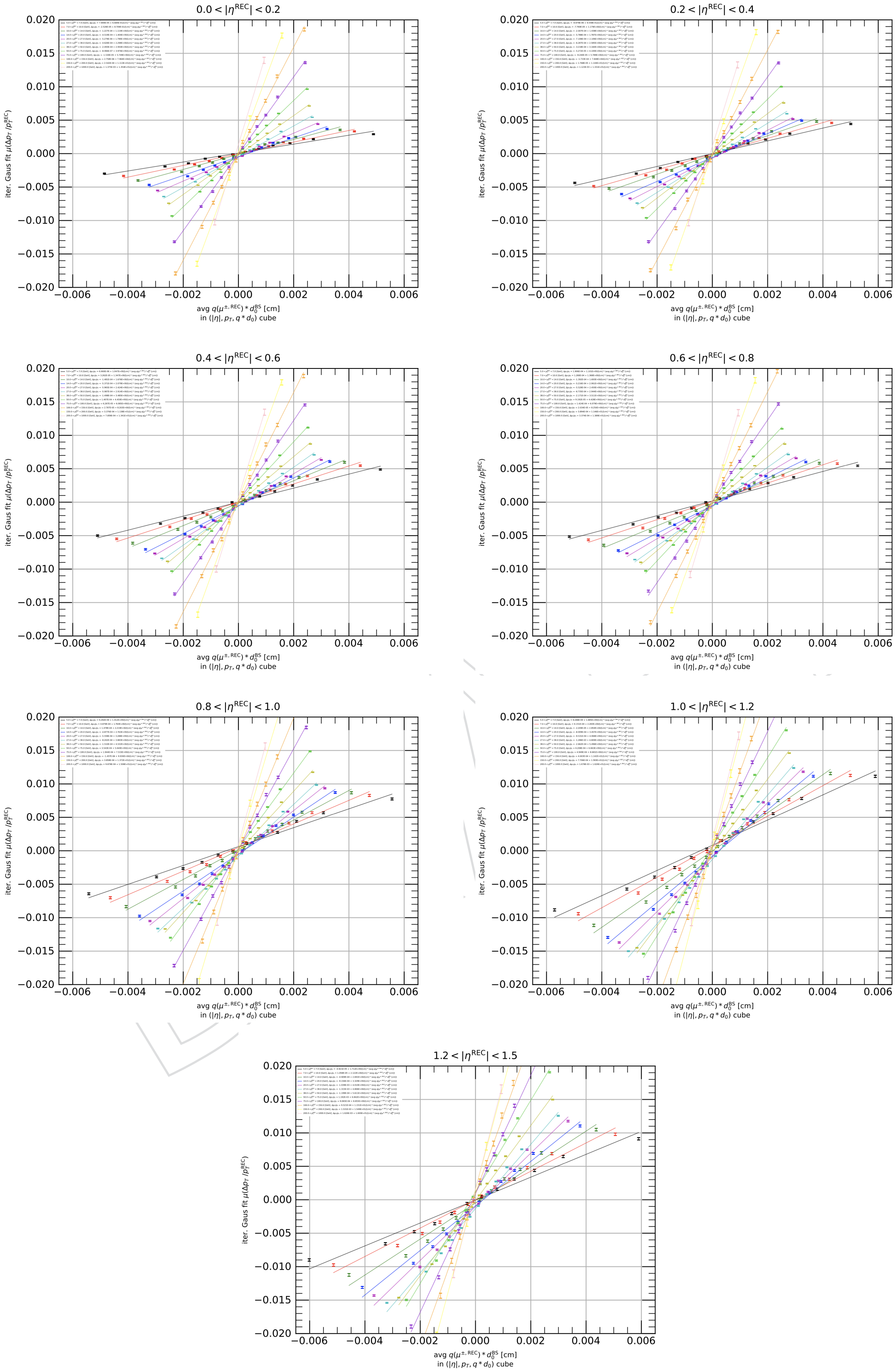

Figure 36: Graphs of $\Delta p_{\mathrm{T}}/p_{\mathrm{T}}$ vs. $\mathrm{avg}(qd_0)$ for each $|\eta|$ bin using 2018 MC. The $|\eta|$ bin edges shown above are: $[0.0, 0.2, 0.4, 0.6, 0.8, 1.0, 1.25, 1.5]$. Each line uses data from a single p_{T} bin. The p_{T} correction parameters for each ($|\eta|$, p_{T}) bin are found in the legend.

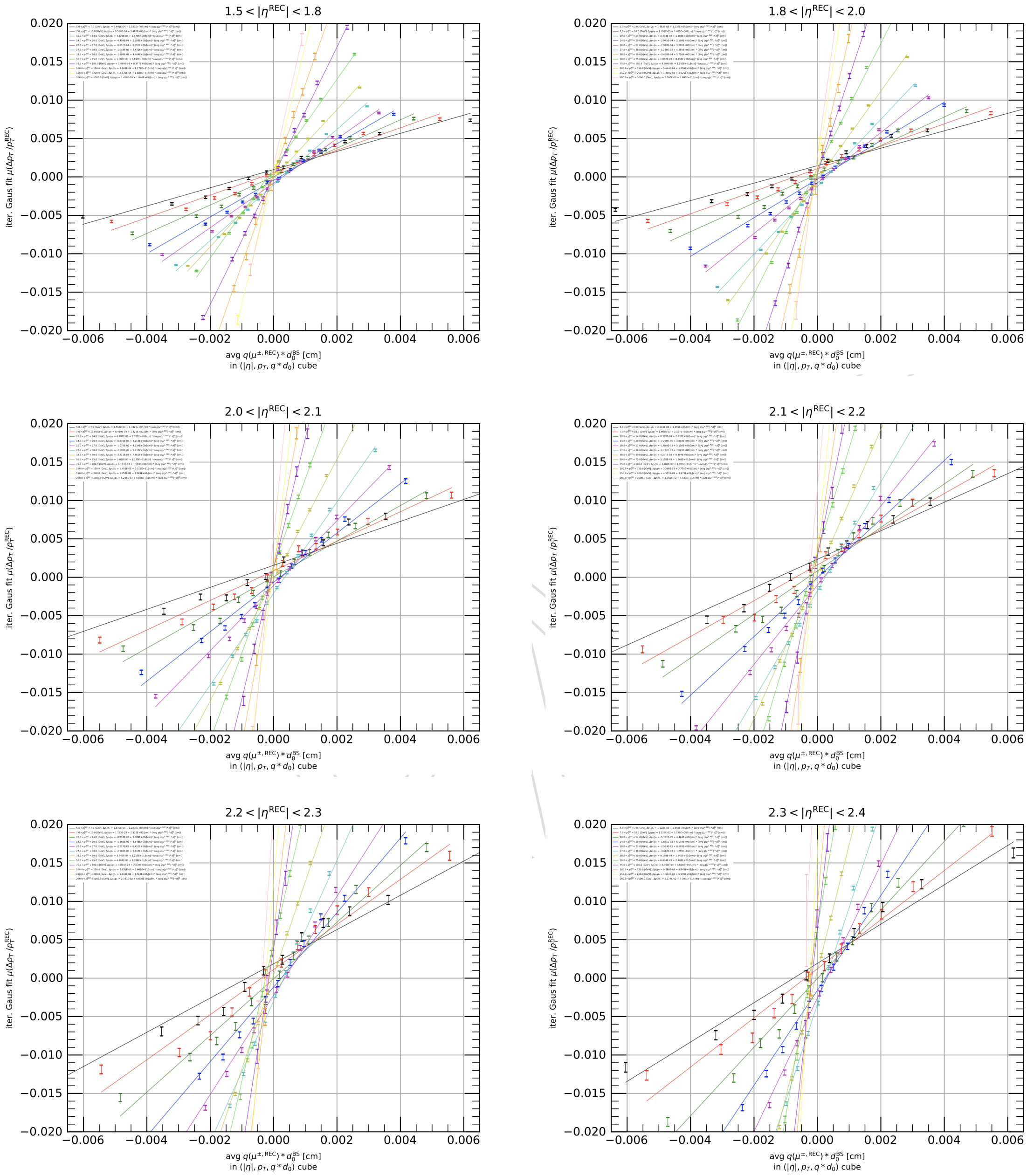

Figure 37: Graphs of $\Delta p_{\mathrm{T}}/p_{\mathrm{T}}$ vs. $\mathrm{avg}(qd_0)$ for each $|\eta|$ bin using 2018 MC. The $|\eta|$ bin edges shown above are: $[1.5, 1.75, 2.0, 2.1, 2.2, 2.3, 2.4]$. Each line uses data from a single p_{T} bin. The p_{T} correction parameters for each ($|\eta|$, p_{T}) bin are found in the legend.

B Impact of a vertex constraint